

# Inferring Photospheric Velocity Fields Using Combination of Minimum Energy Fit, Local Correlation Tracking and Doppler Velocity

B. Ravindra, D.W. Longcope

*Department of Physics, Montana State University  
Bozeman, Montana*

W. P. Abbett

*Space Sciences Laboratory, University of California, Berkeley, CA 94720-7450*

## ABSTRACT

The minimum energy fit (MEF), a velocity inversion technique, infers all components of the photospheric velocity that are consistent with the induction equation. From the set of consistent velocity fields, it selects the smallest overall flow speed by minimizing a kinetic energy functional. If partial velocity information is available from other measurements it can be incorporated into the MEF methodology by minimizing the squared difference from that data. We incorporate the partial velocity information provided by Local Correlation Tracking (LCT) technique and by Doppler velocity measurements. We test the incorporation of these auxiliary velocity fields using the simulated magnetograms and velocitygrams. To the known velocity field we compare the results obtained from the MEF alone, the MEF with LCT constraints and the MEF with LCT and Doppler information. We find that the combination of MEF with LCT and vertical velocity yields the best agreement. We also apply these three methods to actual vector magnetograms of AR 8210, obtained by the Imaging Vector Magnetograph. The results suggest that in this active region the helicity and energy fluxes are dominated by the horizontal rather than the vertical components of the velocity.

*Subject headings:* Velocity Fields, Magnetic Fields, Active Region

## 1. Introduction

As observations and models of the solar magnetic field become ever more sophisticated it has become increasingly desirable to map the plasma velocity across the photosphere.

This velocity drives changes in the magnetic field, in a manner well characterized by the induction equation. Complementary maps of magnetic and velocity fields can be used to calculate the energy flow into the corona: the Poynting flux. The two can also be combined to calculate how twisted the field is becoming, as quantified by its relative helicity of the coronal field (Berger 1984). One possible use for the two complementary maps would be as lower boundary conditions for numerical solutions of the evolving coronal magnetic fields.

The photospheric velocity field was first inferred from the evolution of the photospheric magnetic field by Chae (2001). The local correlation tracking algorithm (LCT November & Simon 1988) was applied to a sequence of maps of a single magnetic field component (line-of-sight magnetograms) to map the horizontal velocity. While the LCT is not strictly equivalent to the induction equation (see Welsch et al. 2004; Longcope 2004; Schuck 2006, for extended discussions of this point) the method has been used extensively to infer photospheric motion in evolving active regions (Moon et al. 2002a; Nindos et al. 2003). It has also been hypothesized (Démoulin & Berger 2003) that the horizontal velocity field,  $\mathbf{u}_h$ , derived in this way is related to the full velocity field  $\mathbf{v}$  as

$$\mathbf{u}_h = \mathbf{v}_h - \frac{\mathbf{B}_h}{B_z} v_z \quad , \quad (1)$$

where  $\mathbf{B} = \mathbf{B}_h + B_z \hat{\mathbf{z}}$  is the local magnetic field vector. Under this assumption the change in coronal helicity is,

$$\frac{dH_R}{dt} = -2 \int_{z=0} (\mathbf{u}_h \cdot \mathbf{A}_p) B_z dx dy \quad , \quad (2)$$

where  $\mathbf{A}_p$  is the vector potential generating the potential (current-free) magnetic field. Thus the horizontal flow field inferred from one component (the line-of-sight component) of the magnetic field is sufficient information to calculate changes to the entire coronal magnetic field.

In order to infer all three components of the velocity field it is necessary to measure changes in all three components of the magnetic field. Vector magnetograms (Stenflo 1994) are maps, now made routinely, of all three magnetic field components at the solar photosphere. Welsch et al. (2004) and Longcope (2004) have developed methods whereby sequence of vector magnetograms are used to infer the velocity vector field. The inductive local correlation tracking method (ILCT Welsch et al. 2004) uses the horizontal LCT field (using Fourier method, called as FLCT, Welsch & Fisher (2007)),  $\mathbf{u}_h$  along with the local magnetic field vector, in conjunction with eq. (1) to calculate the velocity vector  $\mathbf{v}$ . The minimum energy fit (MEF) method (Longcope 2004) begins by seeking a velocity field which exactly satisfies the induction equation for the observed magnetic field evolution. It turns out that there are an infinite number of velocity fields which satisfy this condition. The MEF chooses

from these by demanding that the flow field minimize a penalty function designed to produce desirable properties in the velocity, such as small flow speeds.

Recently these methods, and five others, were tested against a known magnetic evolution (Welsch et al. 2007). A three-dimensional MHD simulation of an rising magnetic flux tube was used to generate a synthetic sequence of vector magnetograms. These were used as input data in the velocity inversion methods, and the results compared to the actual flow present in the simulation. Among the results of this test, the MEF was found to accurately estimate the flow using only the evolving magnetic field. When this inferred velocity field was used to calculate the flux of energy or helicity across the photosphere it produced extremely accurate results: the value agreed well with the one actually known from the simulation.

The MEF derives a velocity field consistent with the evolving magnetic field through the induction equation. This consistency is particularly desirable when the resulting velocity field is used in a numerical simulation which uses that equation. In this way magnetic measurements can be used to infer all components of the velocity field. They are not, however, the only source of velocity data. Doppler measurements are a much more direct measure of the component of velocity along the line-of-sight. A Doppler velocity found in the process of measuring the magnetic field is even directly related to the flow field driving magnetic changes (Chae et al. 2004). It is therefore worth developing a method of incorporating such data into existing velocity inversion techniques.

The penalty functions used in the MEF method provide a natural framework whereby auxiliary information, such as Doppler velocities, might be incorporated (Longcope 2004). The velocity field is still required to satisfy the induction equation, but instead of choosing one with the smallest overall flow speeds, one is sought to most closely match the other data. Doppler maps, called velocitygrams, can be used as constraints on the line-of-sight component of the solution. Since the LCT is not directly used by the MEF, it may be used to constrain the velocity components in the plane of the sky. It is natural to expect that using auxiliary data will naturally produce a more accurate velocity field.

This use of auxiliary data was envisioned by Longcope (2004) in the original presentation of the MEF. Nevertheless, it has not been established through testing that it produces a velocity field any more accurate than the straightforward velocity inversion schemes already in use. The present work performs such tests using the same synthetic magnetogram sequence used in Welsch et al. (2007). We find, as expected, that using both forms of auxiliary data, velocitygrams and the LCT, improves the accuracy of the inferred velocity.

With evidence of its greater accuracy we demonstrate that the combination can be effectively used in real data. Data of all three forms, vector magnetogram sequences, LCT

flows and velocitygrams, are brought together from a single well-studied active region NOAA 8210 from 1 May 1998. We present, using this example, the methodology required to combine these in the MEF. Doing so provides a good estimation of the energy flux and helicity flux into this particular region.

This paper is organized as follows. In the next section we review the MEF and how it may incorporate constraints from auxiliary data. In the following section we feed the synthetic magnetogram sequence into the MEF with no constraints, with just the LCT, and with both the LCT and velocitygrams. The resulting velocities are compared to the actual flow from the simulation. In section 4, the resulting velocities are used to derive integral values, including the energy flux, the helicity flux and the mass flux. The velocity prediction incorporating both LCT and velocitygrams fares best in all these comparison. In section 5 all three methods are applied to the data from AR 8210.

## 2. Minimum Energy Fit with observational constraints

Due to the generally large values of the conductivity in the solar atmosphere, the magnetic field is expected to evolve according to the ideal induction equation

$$\frac{\partial \mathbf{B}}{\partial t} = \nabla \times (\mathbf{v} \times \mathbf{B}) . \quad (3)$$

Since present observational techniques do not provide vertical resolution of either magnetic field or velocity, only the vertical component of eq. (3) within a single plane, the photosphere, can be applied to data.

When all components of the time-evolving magnetic field are known in the photospheric plane, eq. (3) places constraints on the velocity field in that same plane. This is the basis of the Minimum Energy Fit (MEF) model developed by Longcope (2004). It turns out that multiple velocity fields are consistent with the induction equation. To overcome this non-uniqueness the MEF selects one velocity field by requiring that it minimize a penalty function. Given no information aside from the magnetic evolution, the penalty function can involve only the velocity itself. Longcope (2004) chooses the functional

$$W = \frac{1}{2} \int_M (|\mathbf{v}_h|^2 + v_z^2) ds \quad (4)$$

where,  $\mathbf{v}_h$  and  $v_z$  are the horizontal and vertical component of the inferred velocity. The effect of this choice is to select the velocity field with the smallest overall speed which is consistent with the induction equation. The  $\mathbf{v}$  found this way will always be perpendicular to  $\mathbf{B}$  across the entire photospheric surface.

Other measurements, such as dopplergrams, can provide new information which can be used to further constrain the photospheric velocity. We express by  $\mathbf{u}_h$  and  $u_z$  the horizontal and vertical velocity components derived independent of the induction equation. We continue to demand that the induction equation be satisfied exactly, but also minimize a penalty functional incorporating the additional information

$$W = \frac{1}{2} \int_M (|\mathbf{v}_h - \mathbf{u}_h|^2 + |v_z - u_z|^2) ds. \quad (5)$$

If the otherwise-derived velocity  $\mathbf{u}$  were actually consistent with the induction equation then it would be possible to make  $W = 0$  by choosing  $\mathbf{v} = \mathbf{u}$ . In general, however, the other measurements will conflict with the induction equation and this absolute minimum will not be achievable.

An independent constraint on the horizontal velocity can be obtained from the LCT velocities. Démoulin & Berger (2003) consider the LCT-measured velocity to be a tangential component of the plasma velocity modified by the vertical component as in eq. (1). This argument is purely geometrical and there is no rigorous mathematical and observational proof to establish it. Hence, while incorporating the LCT-measured velocity to constrain the MEF velocity we assume that the computed LCT velocity as a purely tangential rather than a combination of vertical and tangential motion of magnetic footpoints. This means that the LCT velocity is considered in this study as  $\mathbf{u}_h = \mathbf{v}_h^{(FT)}$ , the horizontal component of the magnetic footpoint velocity, but does not necessarily satisfy eq. (1) as suggested by Démoulin & Berger (2003). In spite of its use of magnetic data, the LCT velocity will not be consistent with the ideal induction equation (Welsch et al. 2004; Longcope 2004). We propose to find a flow field which is consistent with ideal induction equation and is closest to the LCT velocity using the MEF. Lacking a constraint of the vertical velocity we set  $u_z = 0$  in functional (5). We hereafter refer to this combination as MEF+LCT.

A constraint on the vertical velocity can be obtained from a map of the Doppler velocities at the photospheric level (e.g. Hart 1954). In truth, the Doppler shift measures the component along the line-of-sight, rather than the vertical. Similarly, the LCT measures velocity in the plane of the sky, perpendicular to the line-of-sight. These can be combined into an estimate of all three components and then expressed in terms of the local horizontal and vertical to provide,  $\mathbf{u}_h$  and  $u_z$ . Using the full vector field in this way provides a method we call MEF+LCT+ $u_z$ .

While incorporating the LCT velocity and Doppler velocity to constrain the MEF generated velocity we assume that LCT measured velocity is almost horizontal which is the pattern velocity of surface features and the Doppler velocity represents the vertical flow. As we have pointed out that the right hand side of eq. (1) is the horizontal velocity of magnetic

footpoints, based on the geometrical reason. The assumption made by Démoulin & Berger (2003) is that the horizontal (pattern) velocity returned when the LCT algorithm is applied to line-of-sight magnetograms exactly matches the velocity of magnetic footpoints. This assumption seems plausible but it is an assumption nevertheless.

If eq. (1) were correct there would be some redundancy between LCT and Doppler measurements. Since Doppler measurements will reveal the presence of a velocity component parallel to the magnetic field, any redundancy must be partial. One advantage of the MEF approach is its ability to accommodate any such redundancy, whether total or partial. The MEF seeks to find a single velocity field which best matches all other data in a least-square sense. Any redundancy means a single field will fit both data sets at once. On the other hand, inconsistency in the redundant data means that the fit will be imperfect. Neither situation will lead to a failure of the MEF algorithm. Keeping this in mind we incorporated the Doppler velocity into the MEF and here, we explore this possibility empirically using the synthetic data.

### 3. Testing of the MEF+LCT+ $u_z$

In order to test the algorithm, we apply it to a time sequence of synthetic magnetograms extracted from a simulation of a buoyant magnetic flux rope rising through a turbulent model convection zone. This dataset is the same one used by Welsch et al. (2007) to test and compare a number of velocity inversion techniques including the MEF. We are therefore able to compare our current tests of the improvements to the MEF with those described in the Welsch et al. (2007) study. The model active region was generated using ANMHD, a code that numerically solves the 3D system of MHD equations in the anelastic approximation (see, e.g., Fan et al. (1999); Abbett et al. (2000) and references therein for a detailed description of this technique and its limitations). As was done in Abbett et al. (2004), an active region-scale magnetic flux rope was inserted near the base of an initially field-free, turbulent Cartesian model convection zone spanning 5.25 pressure scale heights vertically. The system was then allowed to evolve over a number of convective turnover times until a significant amount of magnetic flux reached the upper boundary.

From this dataset, we extract the physical variables along a plane positioned near the top of the computational volume (just below the photosphere). We refer to the magnetic field along this slice as a synthetic magnetogram, and use a pair of these separated by a time interval  $\Delta t$  in the MEF algorithms to derive a velocity field. This velocity field is then compared to the *actual* velocity field in the slice. When implementing the MEF+LCT+ $u_z$  method we use the vertical velocity in the slice as both the dopplergrams *and* the target for

comparison.

Following Welsch et al. (2007) we compare the actual velocity field to the various derived versions in several ways. We compare the different components of the velocity pixel by pixel using a scatter plot. We also compare integral quantities which involve integrals over the slice, such as net vertical flow, Poynting flux and helicity flux. When making these comparisons we vary the time separation,  $\Delta t$ , between magnetograms. Following Welsch et al. (2007) we use intervals  $\Delta t = 250, 753, 1256, 2264, 4284, 8374$  and  $16746$  seconds, centered on a common central time: the fifty-fifth magnetogram in the sequence. The adopted pixel length scale for the simulated magnetogram is  $348$  km.

To compare the velocity fields obtained from each of these methods at different time intervals with the true velocity fields from the simulation, we used the time averaged velocity field corresponding to the time difference between the magnetograms used in the velocity inversion technique. Also, in estimating and comparing the integral quantities we used the time averaged magnetogram.

### 3.1. Inferred flow fields

To the pairs of synthetic magnetograms described above we apply the simple MEF, LCT, MEF+LCT and MEF+LCT+ $u_z$ . Since all versions of the MEF can be applied only to regions of sufficiently strong magnetic field we extract the central portion of the magnetogram by adopting a mask with a threshold on the magnetic field of magnitude  $170$  G. The extracted portion consists of bipoles with strongest magnetic field at the edges of the mask as shown in Figure 1(left). The corresponding velocity field in the masked region is shown on right side of Figure 1.

We first applied the MEF alone to a pair of vector magnetograms to infer the components of the velocity fields. We employed a simple multi-grid strategy to speed to convergence of this iterative method. We first interpolated the magnetograms onto a coarser grid, typically of one-quarter the original resolution, and applied the MEF. The resulting velocity information and magnetograms are interpolated to a finer grid and used as an initial guess for the MEF. These results are interpolated to the next coarsest grid (that is one-half of the original resolution) and the process repeated. After a few such iterations (typically 2-3) the output velocities are interpolated to the original grid sizes and is the inferred flow field.

To infer the horizontal flow fields we used the LCT on the vertical magnetograms. After some experimentation we chose a Gaussian apodizing window function of size  $15$ – $22$  pixels depending upon the time difference between the two magnetograms; larger apodizing

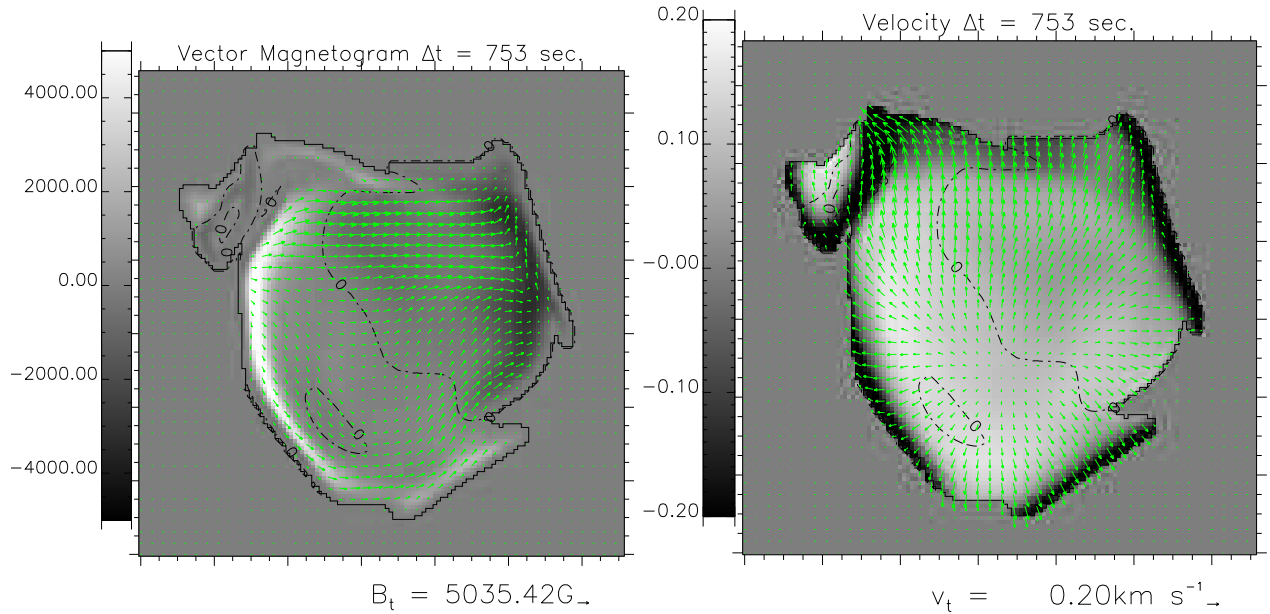


Fig. 1.— A sample magnetogram (left) and velocitygram (right) extracted from the time series of simulated magnetograms and velocitygrams. The contours separate the magnetic and non-magnetic regions. The contour with zeros in between the bipole indicates the position of the magnetic neutral line. The vertical magnetic field strength is shown in the bar and the size of the arrow in the bottom of the figure represents the magnitude of the transverse magnetic field. Similarly the magnitude of the vertical flow is shown in the bar and the size of the arrow represents the magnitude of the transverse velocity.

windows are used in conjunction with larger  $\Delta t$ . These LCT velocities are used as  $\mathbf{u}_h$  in the penalty function (5), while  $u_z = 0$ . We used the multi-grid procedure as described above to obtain a converged velocity field  $\mathbf{v}$ .

In order to test the MEF+LCT+ $u_z$  algorithm, the vertical velocity field,  $u_z$ , is extracted from the true flow field for the corresponding time steps. For the particular time step we averaged over a pair of velocity images. We converted the velocity ( $\text{m s}^{-1}$ ) to displacement, in pixels, to match all other input and output quantities.

Figure 2 shows the inferred horizontal velocity vectors ( $\mathbf{v}_h$ , green arrows) obtained from the LCT (top left), MEF (top right), combination of MEF+LCT (bottom left) and MEF+LCT+ $u_z$  (bottom right) overlaid, except in the case of LCT, upon the vertical velocity field ( $v_z$ , grey scale). In the case of LCT, which does not produce a vertical flow, the grey-scale shows the vertical component of the magnetic field. In all cases the direction of these inferred flow fields compare favorably with those with the true flow fields (Figure1 (right)).

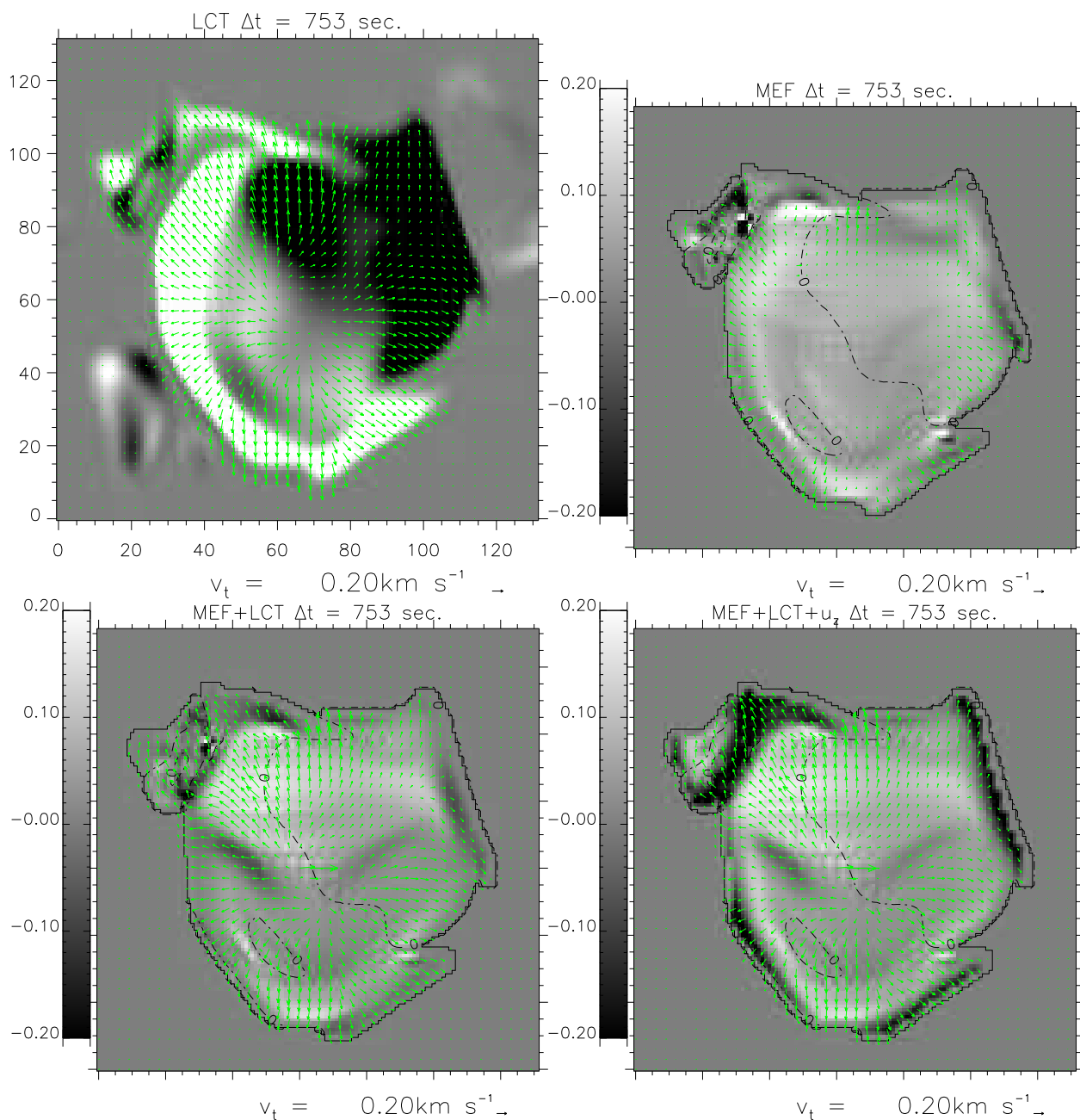


Fig. 2.— The flow fields inferred using LCT (top left), MEF (top right), combination of MEF+LCT (bottom left) and MEF+LCT+ $u_z$  (bottom right) velocity inversion techniques are shown for a magnetogram pairs with  $\Delta t = 753$  sec. The LCT velocity vectors (top left) are overlaid upon the vertical component of the magnetic field (grey scale). All other velocity vectors are overlaid on the inferred vertical component of the flow field (grey scale). In all these maps, the strength of the vertical flow is shown on the vertical bar and the size of the arrow represents the magnitude of the horizontal flow field.

Similar results were obtained for different time gaps between the magnetograms (see Welsch et al. 2007; Ravindra & Longcope 2007).

All techniques involving the MEF are capable of inferring a vertical flow,  $v_z$ , given only the evolution of the vertical magnetic field. The vertical flow inferred from the MEF, MEF+LCT and MEF+LCT+ $u_z$  show strong upflow in the center as in the true flow fields. The vertical flow inferred by the hybrid technique (MEF+LCT+ $u_z$ ) is, however, in better agreement with the true vertical flow. There are vertical downflows at the edges undetected by the MEF and MEF+LCT. This inadequacy is due in part to the fact that MEF can infer only the velocity which is perpendicular to the magnetic field (Longcope 2004).

Figure 3 shows the quantitative comparison of the magnitude of the inferred velocity using LCT (top left), MEF (top right), MEF+LCT (bottom) and MEF+LCT+ $u_z$  (bottom right) with the true flow fields which includes both the field aligned and perpendicular components. From the scatter plots it is evident that there is larger scatter in the values returned by the MEF. The LCT and MEF+LCT return horizontal velocity components with better correlation. The MEF+LCT+ $u_z$  produces results intermediate to the other three. All scatter plots show that LCT, MEF+LCT and MEF+LCT+ $u_z$  recover the horizontal velocity close to the original. The MEF+LCT+ $u_z$  recovers the vertical component of the velocity better than other techniques. This is not altogether surprising since the actual value is used as an input. It should be noted here that MEF recovers a velocity perpendicular to the magnetic field. In contrast to Welsch et al. (2007), we are comparing these velocity magnitudes with the full velocity of the actual flow field (field aligned as well as perpendicular).

### 3.2. Comparisons of actual and reproduced time derivative

All techniques are designed to make the quantity  $[\nabla \times (\mathbf{v} \times \mathbf{B})]_z$  match the Eulerian time derivative  $\partial B_z / \partial t$  calculated from a pair of magnetograms. This fact is illustrated in Figure 4, whose top left image is a true derivative,  $\partial B_z / \partial t$ , and whose other panels show the derived quantity designed to match it. The derivatives are computed using 3-point interpolation. Apart from the high spatial frequency components, all the computed fields compare favorably with the true time derivative. The high frequency components are due to the small magnetic field strength at the neutral line and along the border of the magnetograms (see Longcope 2004). These time derivative maps are obtained by using the velocity and magnetic fields at a time difference of 753 sec. The maps are similar at all the time intervals.

Figure 5 shows pixel-by-pixel scatter plots of the time derivatives for the different velocity inversion methods is plotted against the true time derivative obtained from the true

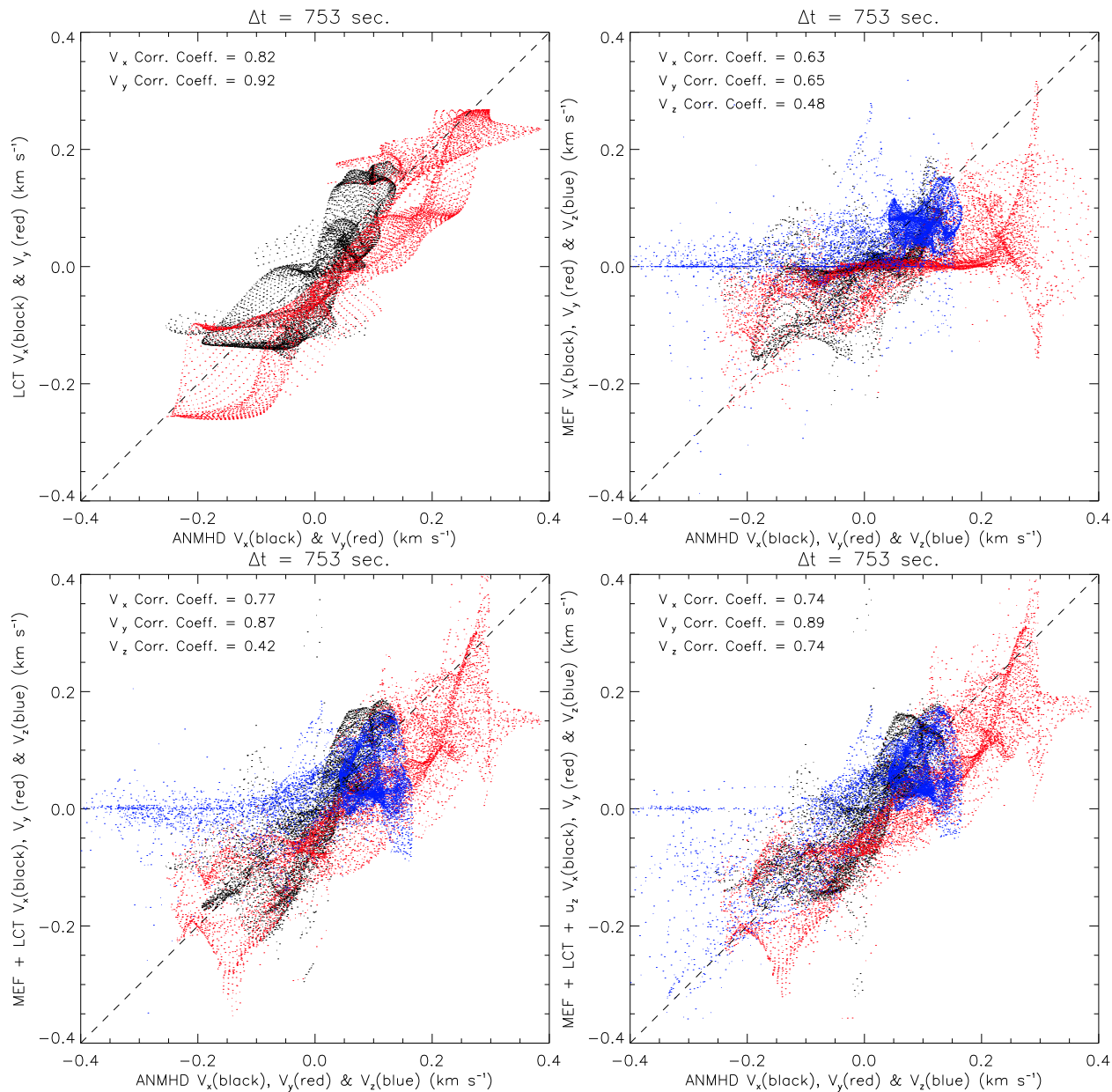


Fig. 3.— Scatter plots of the magnitude of the inferred flow components vs the magnitude of the true flow components. These flow components are inferred from the LCT (top left), MEF (top right), MEF+LCT (bottom left) and MEF+LCT+ $u_z$  (bottom right) velocity inversion techniques. In all these plots the color black, red and blue corresponds to  $v_x$ ,  $v_y$  and  $v_z$  velocity magnitudes respectively.

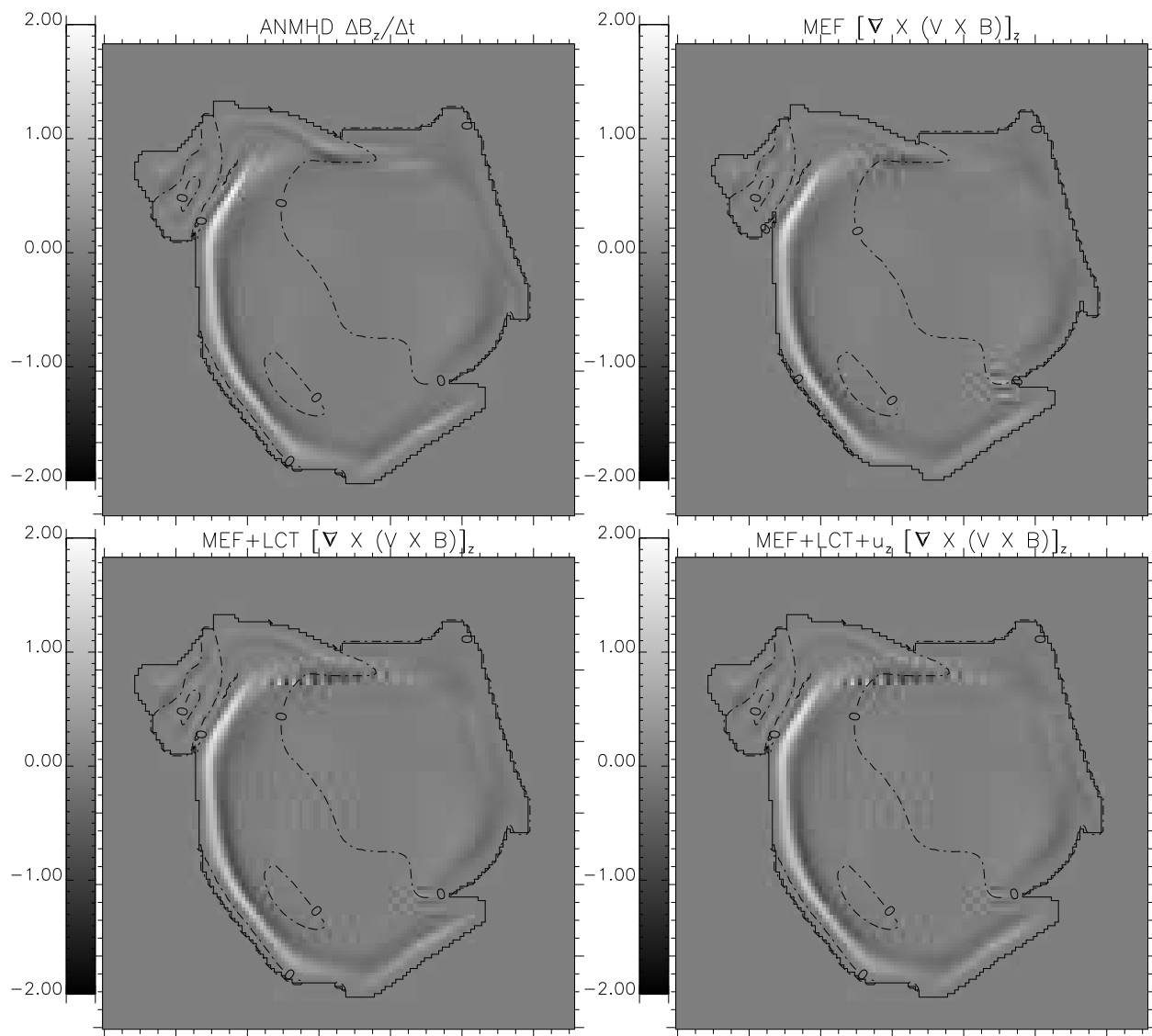


Fig. 4.— (Top left) Map of time derivative of  $B_z$  separated by a time difference of 753 seconds is shown. The map of computed time-derivative obtained by using the velocities of MEF (top right), combination of MEF+LCT (bottom left) and MEF+LCT+ $u_z$  (bottom right) are also shown. The gray scale vertical bar shows the magnitude of the temporal derivatives in units of  $\text{G s}^{-1}$ .

magnetogram and velocity fields with a same time difference. All the plots shown here are for the time difference of 753 seconds. Similar plots were obtained for all the time difference. From these plots it is evident that there is a good correlation between the true and reproduced temporal variations. The fitted slope is computed using IDL's least abso-

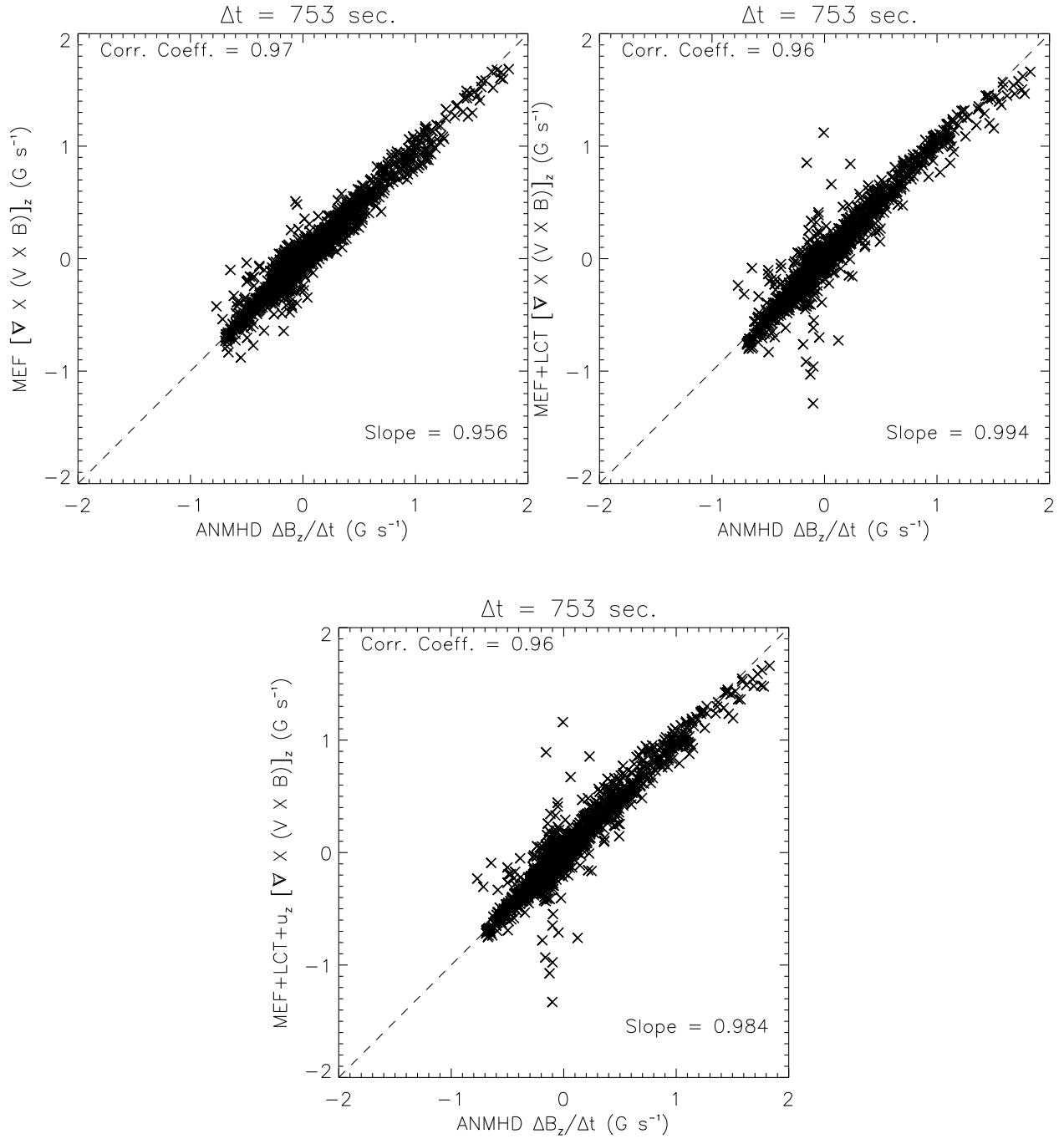


Fig. 5.— Scatter plot between actual and reproduced time-derivatives is shown. The velocity components used in the reproduced temporal variations are obtained from the MEF (top left), MEF+LCT (top right) and MEF+LCT+ $u_z$  (bottom) velocity inversion techniques.

lute deviation technique and it is found to be close to one, suggesting that all the velocity components indeed follow the induction equation.

#### 4. Comparisons of integrated quantities *vs.* $\Delta t$

It is important to characterize how the performance of these methods depends on the time interval,  $\Delta t$ , between magnetograms. All methods approximate the time derivative,  $\partial B_z/\partial t$ , using a finite difference,  $\Delta B_z/\Delta t$ . This approximation will be most accurate for small time intervals and will become invalid when  $\Delta t$  exceeds the characteristic time scale for flux evolution (several hours on active region scales). On the other hand, were noise present in the magnetograms its contribution to  $\Delta B_z$  would not scale with  $\Delta t$  while the actual value (i.e. the signal) would scale linearly. For higher signal-to noise it is therefore desirable to operate with *larger* time intervals. Furthermore, LCT has difficulties detecting displacements much smaller than one pixel using cross-correlations between pixelated images. Its performance therefore also deteriorates at small  $\Delta t$  (Fisher & Welsch 2007).

To explore the performance of the methods with  $\Delta t$  we compare integral quantities such as net vertical flow, Poynting flux and helicity flux. These quantities are significant contributors to coronal dynamics, so they are valuable measures by themselves. For each comparison we perform the inversion on magnetograms separated by  $\Delta t$ , to produce a single velocity field  $\mathbf{v}$  attributed to the center of the time interval. For self consistency we combine this with a magnetic field found by averaging the time-separated magnetograms. The true velocity fields from the simulation corresponding to  $\Delta t$  intervals are averaged and are taken as the true flow fields.

##### 4.1. Net vertical flow

The net vertical flow is calculated by integrating the vertical flow field over all pixels,

$$F_z = \int v_z(x, y, 0) dx dy \quad . \quad (6)$$

This quantity, with units of volume per time, could in principle be multiplied by a mass density to obtain mass flow across the photospheric level. Since we derive the quantity using magnetic evolution it actually represents the net amount of emergence or submergence occurring within the magnetized region. The synthetic data set is derived from a simulation of flux *emergence* for which  $F_z > 0$ . There are, however, downflows ( $v_z < 0$ ) at the perimeter of the emerging flux which partially diminish  $F_z$ . The overall accuracy with which the

inversion method captures this behavior is characterized by its inferred  $F_z$ .

Figure 6 compares the net vertical flows computed using various combinations of velocity recovery techniques with the true net vertical flow. The true net vertical flow is naturally independent of  $\Delta t$ . The plot shows that the net vertical flow computed from the combination of MEF+LCT+ $u_z$  compares favorably (a little larger in value) with that of the true flow in the beginning and at large time difference (larger than 8374 seconds) the difference in the values are large. The result is, once again, unsurprising given that the actual upflow is used as an input. The MEF and MEF+LCT over-estimate the net vertical flow. This over-estimation is another consequence of the fact that MEF can infer only the perpendicular component of the true flow. It was noted previously that this led to its missing the region of downflows, which are largely field-aligned. The simulations capture the well-known tendency for mass advected into the corona by emerging flux to subsequently drain back along the field lines. We therefore expect that MEF is likely to systematically overestimate vertical flux. Only by incorporating an independent measurement of vertical flow, such as a dopplergrams, can this be corrected. Figure 6 shows that MEF+LCT+ $u_z$  succeeds at this, but not fully.

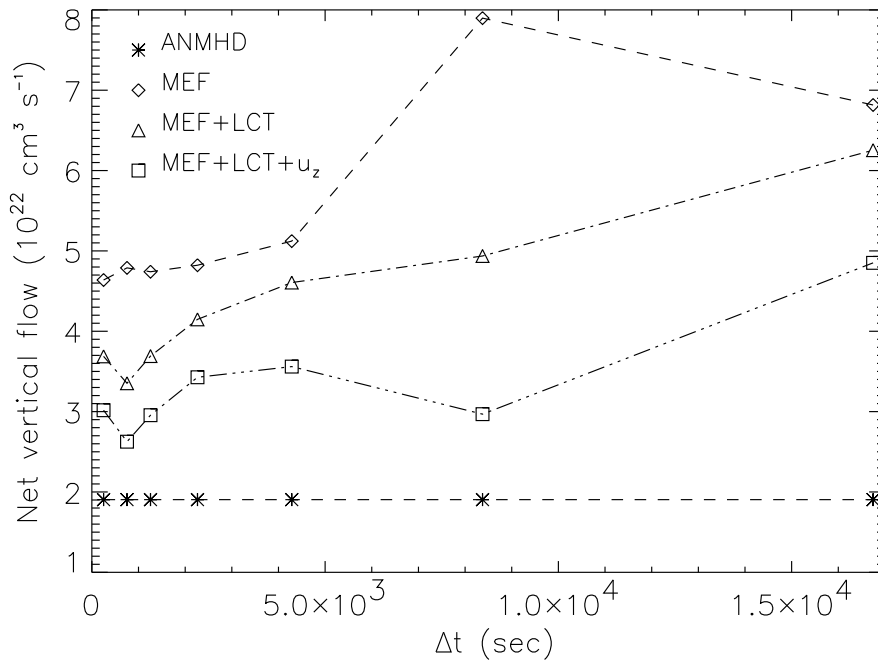


Fig. 6.— The net vertical flow inferred from MEF ( $\diamond$ ), MEF+LCT ( $\triangle$ ) and MEF+LCT+ $u_z$  ( $\square$ ) velocity inversion techniques are plotted as a function of time. The true net vertical flow (ANMHD in the plot) is also shown for comparison.

## 4.2. Poynting flux

The flux of magnetic energy transferred into the solar corona is given by the integrated Poynting flux

$$\dot{E} = \frac{1}{4\pi} \int_s B_h^2 v_z dx dy - \frac{1}{4\pi} \int_s (\mathbf{v}_h \cdot \mathbf{B}_h) B_z dx dy . \quad (7)$$

The first term on the right hand side (rhs) arises from the emergence (or submergence) of magnetic energy across the photosphere, while the second is due stressing of the field by shearing of magnetic footpoints. Figure 7 compares the integrated Poynting flux using different velocity inferring techniques as a function of  $\Delta t$ . The plot shows that the energy flux obtained from all MEF methods matches the actual flux very well. The MEF+LCT+ $u_z$  matches most closely, the MEF and MEF+LCT are slightly smaller than the the actual value. The LCT alone grossly underestimates the integrated Poynting flux, suggesting that the emergence contribution to Equation (7) is dominant in the present case. The true net Poynting flux decreases with interval  $\Delta t$ . The Poynting flux estimated using the MEF+LCT+ $u_z$  also decreases with time interval but for intervals greater than 8374 seconds the estimated Poynting flux differs from the true flux, indicating that the inferred velocities are too far from the true velocities at large time differences.

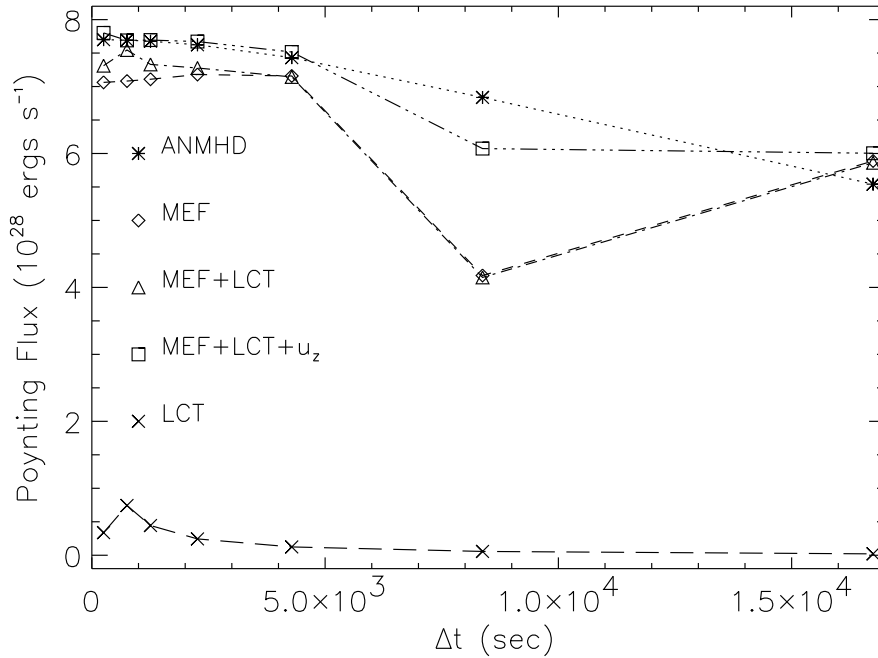


Fig. 7.— Poynting flux estimated using various velocities are plotted along with the true Poynting flux as a function of time.

### 4.3. Helicity fluxes

The relative helicity is an integral over the entire coronal half-space  $z > 0$  which characterizes the net twisting of coronal field lines about one another (Berger 1984). Assuming the coronal plasma obeys the ideal induction equation the coronal helicity can change only through motions at the photospheric boundary. Its rate of change is given by the integral

$$\dot{H} = 2 \int_{z=0} (\mathbf{A}_p \cdot \mathbf{B}_h) v_z dx dy - 2 \int_{z=0} (\mathbf{A}_p \cdot \mathbf{v}_h) B_z dx dy , \quad (8)$$

where  $A_p$  is the vector potential generating the potential (current-free) magnetic field; it is subject to several conditions (Berger 1984). The first term on the rhs of Equation (8) captures the transport of helicity into the corona by emergence across the photosphere. The second term quantifies the helicity injected as photospheric motions braid magnetic footpoints about one another. Démoulin & Berger (2003) demonstrated that both terms in expression (8) could be replaced by a single term similar to the braiding (second) term but involving  $\mathbf{u}_h$  found from LCT as in eq. (2). This assumed that  $\mathbf{u}_h$  represented in eq. (1) is not just the horizontal velocity but the *apparent* motion of magnetic footpoints, called the flux transport velocity (Welsch et al. (2007)). Since the MEF methods recover all components of  $\mathbf{v}$  we calculate helicity flux using expression (8). The LCT alone does not return a value of  $v_z$ , so we compute only the second term. If its value actually reflects all components according to eq. (1) then the second-term value of eq. (8) should match the actual helicity flux.

Figure 8 shows the total helicity flux as a function of  $\Delta t$ . All methods (except the LCT at small time difference) agree on the negative sign of the flux, which arises from the emergence of a flux rope with left-handed twist. The helicity fluxes obtained from the MEF alone compare favorably with the true helicity fluxes except at large time difference. The helicity fluxes obtained from the MEF+LCT and the MEF+LCT+ $u_z$  are smaller than the true values. Notably the helicity flux obtained from LCT alone is an order of magnitude smaller than the true value. This discrepancy suggests that the LCT returns a horizontal velocity different from eq. (1). To examine this, we incorporated the true magnetic and velocity fields obtained from the simulation corresponding to  $\Delta t=753$  sec. into the eq. (1). The resulting flux transport velocity is found to be more than ten times larger than the LCT measured velocity in places around the neutral line. The flow field from eq. (1) (not shown) appears to diverge away from the neutral line, and is generally parallel to the transverse field,  $\mathbf{B}_h$ . In contrast to this the LCT velocity more closely resembles the true horizontal velocity field,  $\mathbf{v}_h$ , in both magnitude and direction (cf. Figure 2 & Figure 3). As a consequence the helicity fluxes obtained from the LCT velocity is smaller than the actual helicity flux and is close to the second integral on the right hand side of eq. (8) alone.

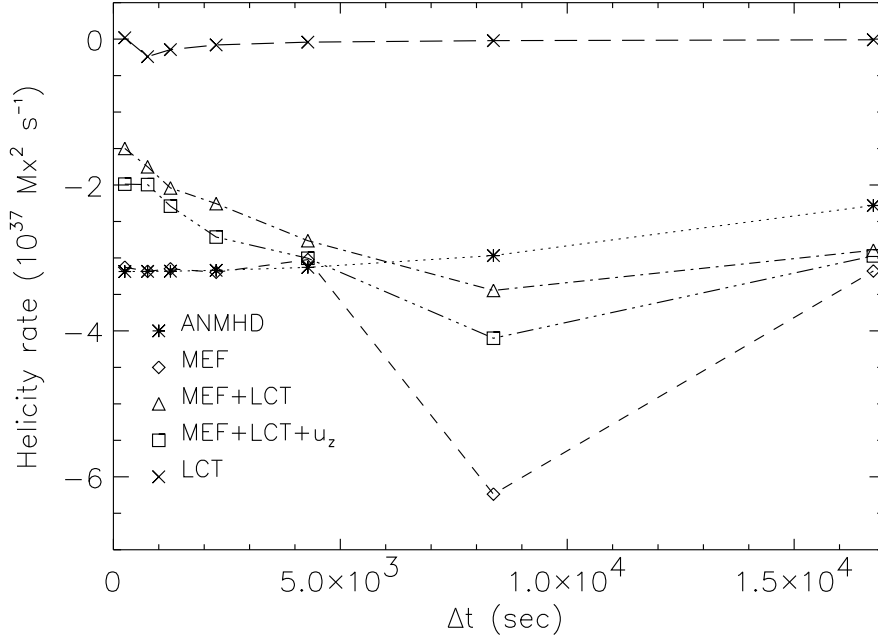


Fig. 8.— The helicity fluxes obtained by using LCT velocity and various combination of MEF algorithm with the other velocities are plotted as a function of time. The true helicity fluxes are also plotted for comparison.

In the true helicity flux, the emergence term (first term on the rhs of eq. (8)) is actually dominant. This is natural in a simulation of a rising twisted flux rope. Figure 9 (left) plots the values of that single term for each of the methods. This contribution is well recovered by the MEF at small time differences and by the MEF+LCT+ $u_z$  at large time difference, which had also best recovered the net vertical flow. The term is systematically smaller in MEF+LCT. The LCT alone does not measure the vertical flow, so it is not plotted. Figure 9 (right) shows the helicity flux due to the shearing motion is positive in their value. The MEF+LCT+ $u_z$  and MEF+LCT is able to recover that for small  $\Delta t$  and larger intervals their magnitude reduces but the sign is generally positive. In contrast to this the helicity due to the shearing motion obtained from the MEF is always negative. The shear term of helicity obtained from the LCT velocity is positive for small intervals and slowly turns negative suggesting that it is not completely recovering the helicity due to shear or the emergence.

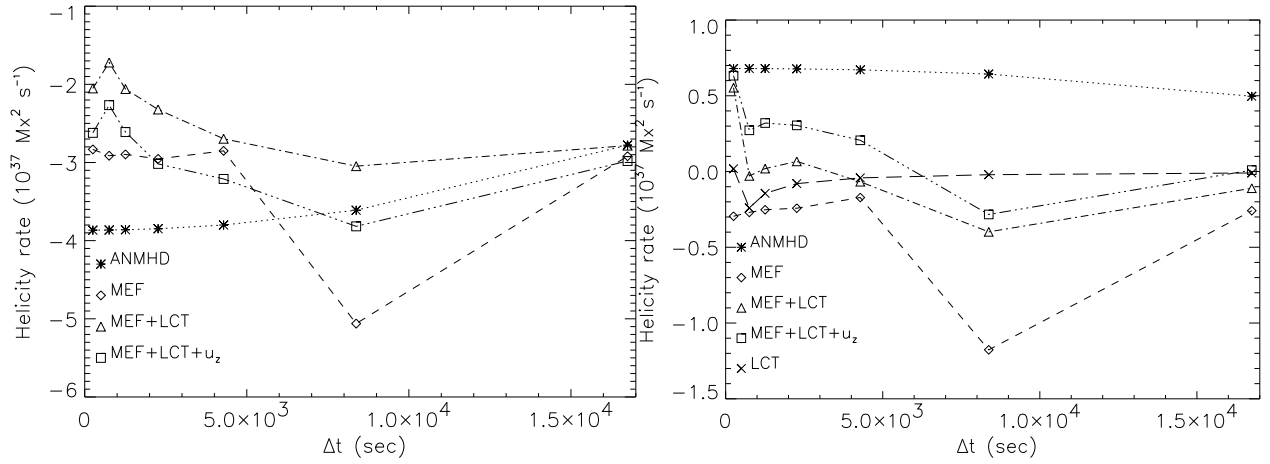


Fig. 9.— (Left) The component of the helicity flux due to emergence/submergence computed using combination of MEF with the various other velocities are plotted as a function of time. (Right) A component of the helicity flux due to the horizontal shearing motion of the magnetic field footpoints is shown for the LCT velocity and also for a combination of the MEF with other velocities.

### 5. Application to real vector magnetogram data: velocity field in AR 8210

We now demonstrate the hybrid MEF techniques on actual vector magnetogram data by applying it to Imaging Vector Magnetogram (IVM Mickey et al. 1996; Labonte et al. 1999) data. We chose the AR 8210 which has been the subject of many previous studies (Warmuth et al. 2000; Sterling & Moore 2001; Pohjolainen et al. 2001; Wang et al. 2002; Xia et al. 2002) including the first application of MEF alone (Longcope 2004). There are theoretical reasons to believe that energy and helicity injection into an active region play a role in flares and CMEs. This particular region was the site of many such events during its central meridian passage as it produced many X-class and M-class flares. A more accurate determination of its photospheric flows could therefore prove useful in observational confirmation of the role of photospheric motions in these events.

The AR 8210 rotated onto the disk on April 25, 1998 on the southern hemisphere, at a latitude of  $17^\circ$ . The AR 8210 is non-Hale-Nicholson region as the negative polarity sunspot in the southern hemisphere is following the positive region. The main sunspot in the active region was observed to rotate at a rate of  $5\text{-}15^\circ \text{ day}^{-1}$  (Warmuth, et al. 2000). It is also observed that the positive polarity region on east side of the spot was moving southward. On May 02, 1998, while it was close to the disk center, this active region produced a X1.1/3B flare at 13:40 UT. Following this flare, a halo CME with a velocity of  $938 \text{ km s}^{-1}$  was ejected

into the interplanetary medium. This particular event was extensively studied by many researchers (e.g., Warmuth et al. 2000, Wang et al. 2002). Before this event on May 1, 1998 the same active region produced a small M1.2 class flare at 22:54 UT which also accompanied with a halo CME with a speed of  $585 \text{ km s}^{-1}$  and a kinetic energy of about  $1.2 \times 10^{31}$  ergs. This particular event was also well studied by Regnier and Canfield (2006) using an IVM dataset similar, but not identical, to the one used here. They estimated the free energy which is ranging from  $1\text{-}5 \times 10^{31}$  ergs. The estimated relative magnetic helicity is negative and it is in excess of  $10^{42} \text{ Mx}^2$ . They also found that a delay of about 20 min. between the energy and helicity injection and response of the corona.

### 5.1. Data used: magnetogram data

On 1 May 1998, the IVM made measurements of Stokes parameters at a 3 minute cadence, within AR 8210 located at S16E02. The observation sequence began at 17:09 UT and ended at 23:27 UT, spanning an interval of 6 hr 18 minute with 4 small data gaps. The  $180^\circ$  ambiguity is resolved according to Canfield et al. (1993); Leka & Barnes (2003). Successive magnetograms were aligned by maximizing the cross-correlation between the two successive intensity images. Random noise in the magnetograms were reduced by averaging the 5 successive co-aligned magnetograms. The pixel resolution of the obtained IVM magnetograms is  $1.1''$

We use pairs of magnetograms separated by 30 minutes in the MEF algorithm to infer the velocity fields. As a first step, we first generated the time averaged magnetic field and the difference magnetic field. Figure 10(left) shows the time-averaged vertical magnetic field overlaid with the transverse magnetic field. The active region has a main negative sunspot surrounded by opposite polarity plage. The negative sunspot has a maximum vertical field strength in excess of  $-3000 \text{ G}$ . The magnetogram difference from the same pair (right of Fig. 10) shows a large amount of variation in the umbra of a sunspot. This fluctuation may be real or due to the introduction of noise by the scattered light; we cannot distinguish between these two. We selected the strong-field sub-region by using a threshold magnetic field strength of  $50 \text{ G}$ . This value avoids the noisy pixels. We have maintained the same sub-region in all the frames.

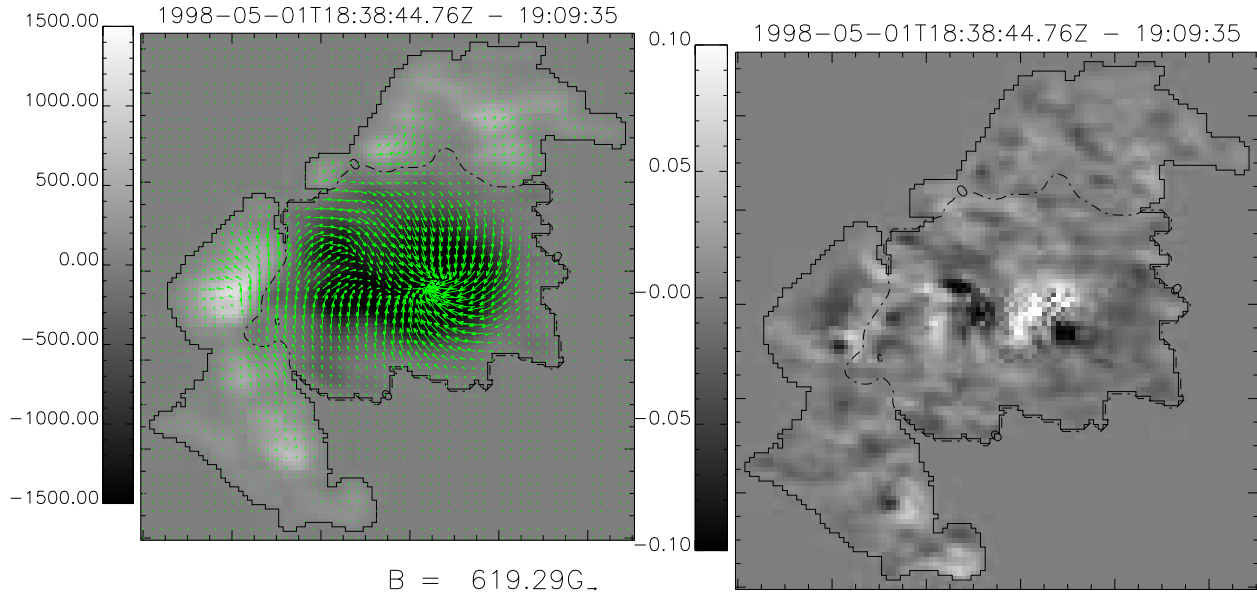


Fig. 10.— (Left side) A map of mean vertical magnetic field overlaid with the horizontal component of the magnetic field vector. The size of the arrow in the bottom of the magnetogram represents the magnitude of the transverse magnetic field. The vertical bar represents the vertical magnetic field strength in Gaussian units. (Right side) A map of temporal difference of vertical component of the magnetic field. The vertical bar on the left side of the image represents the scaling in units of  $\text{G s}^{-1}$ . The title on the top of the image indicates the date and time over which the average and difference magnetic fields are computed.

## 5.2. Dopplergram data

We use dopplergrams as a partial velocity information for the MEF in the manner described in previous sections. We use dopplergram data from Michelson Doppler Imager (MDI Scherrer et al. 1995) on-board the Solar and Heliospheric Observatory (SOHO Domingo et al. 1995) taken at a cadence of 1 minute. The data are full-disk dopplergrams with a pixel resolution of  $1.''98$ . The dopplergrams were co-aligned with the IVM magnetograms by maximizing the cross-correlation between the MDI magnetogram and IVM magnetogram. This procedure includes dilation, rotation and translation of the MDI magnetogram. We then co-aligned the MDI tracked dopplergrams (which are interpolated to IVM image-scale and rotated to IVM orientation) with the MDI magnetogram, which had been co-aligned with IVM. Missing dopplergrams in a time series were interpolated.

Apart from the line-of-sight velocities, the dopplergrams exhibit varieties of other flows and oscillations for which corrections must be made. Solar rotation leads to a large-scale

gradient in Doppler velocity, which we subtracted from each dopplergrams in a time series. Short-lived signals such as 5 minute acoustic oscillations were removed by using weighted average, tapered Gaussian temporal low-pass filter (Libbrecht & Zirin 1986; Hathaway et al. 2000). In this filter, a weighted average over 31 images was taken with a half-width of 8 minutes and half-length of 16 minutes. Evershed flow (Evershed 1909) is a strong horizontal flow which flows radially outward from the sunspot. This Evershed flow is suppressed by subtracting each dopplergram in a time series from the time-averaged dopplergram. The resulting dopplergram shows a large scale velocity field. The obtained dopplergram velocities are converted into shifts interms of pixels so that the LCT and Doppler velocities are in identical units.

### 5.3. Inferred flow fields in AR 8210

We use the LCT algorithm to find a horizontal flow field,  $\mathbf{u}_h$ , for a second constraint. After many trials, we chose a Gaussian apodizing window function of width  $6.6''$  for pair of magnetograms separated by  $\approx 30$  min.

Since the active region is not exactly at disk center ( $\mu \sim 0.96$ ), the Doppler velocity does not coincide with the *vertical* component of the flow velocity. For the same reason the LCT velocity field, in the plane of the sky, is not equivalent to the flow's *horizontal* components. We combine the line-of-sight (Doppler) and plane-of-sky (LCT) components into full vectors, and extract from these their strictly vertical ( $u_z$ ) and horizontal ( $\mathbf{u}_h$ ) components for use in the MEF+LCT+ $u_z$  method. While this particular region might be close enough to disk center to permit this step to be skipped, we perform it in order to demonstrate the technique in its full generality.

The horizontal velocity obtained from the LCT shows (Figure 11 and 12 top left) the clockwise rotation of the main sunspot and anti-clockwise motion of the positive plage region along the east side of the sunspot. These motions are consistent with previous analysis of this region (Warmuth et al. 2000; Welsch et al. 2004). In contrast the MEF velocity shows (Figure 11 and 12 (top right)) a strong anti-clock wise motion in the positive region with the absence of clockwise rotation of the spot. The inclusion of LCT constraint permits the clockwise rotation to be recovered by MEF+LCT (Figure 11 and 12 (bottom left)) and MEF+LCT+ $u_z$  (Figure 11 and 12 (bottom right)).

The vertical flow pattern found by MEF alone is roughly similar to those found by the hybrid methods. There are some exceptional regions found by MEF+LCT+ $u_z$ . This discrepancy arises because the MEF can recover only velocity strictly perpendicular to the

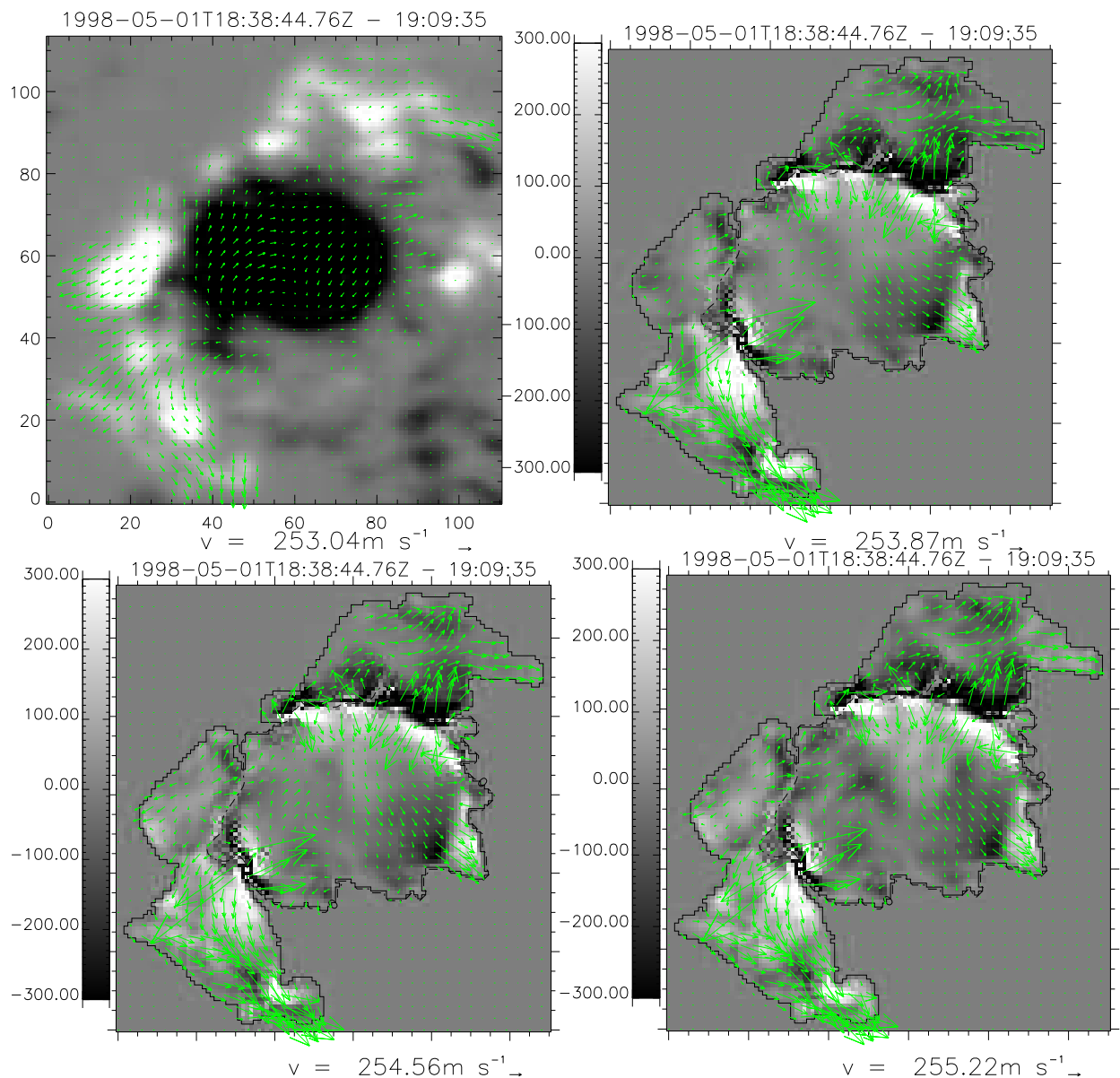


Fig. 11.— The inferred horizontal flow fields in AR 8210 obtained from LCT (top left), MEF (top right), MEF+LCT (bottom left) and MEF+LCT+ $u_z$  velocity inversion techniques overlaid upon the corresponding inferred vertical component of the flow field, except in the case of LCT where it is overlaid on the magnetogram is shown. The size of the arrow in the bottom of the image represents the magnitude of the transverse velocity and the vertical bar on the left side of the image represents the magnitude of the vertical flow fields in units of  $\text{m s}^{-1}$ . The date and time of the pair of magnetograms over which the velocity is inferred is shown on the top of each image.

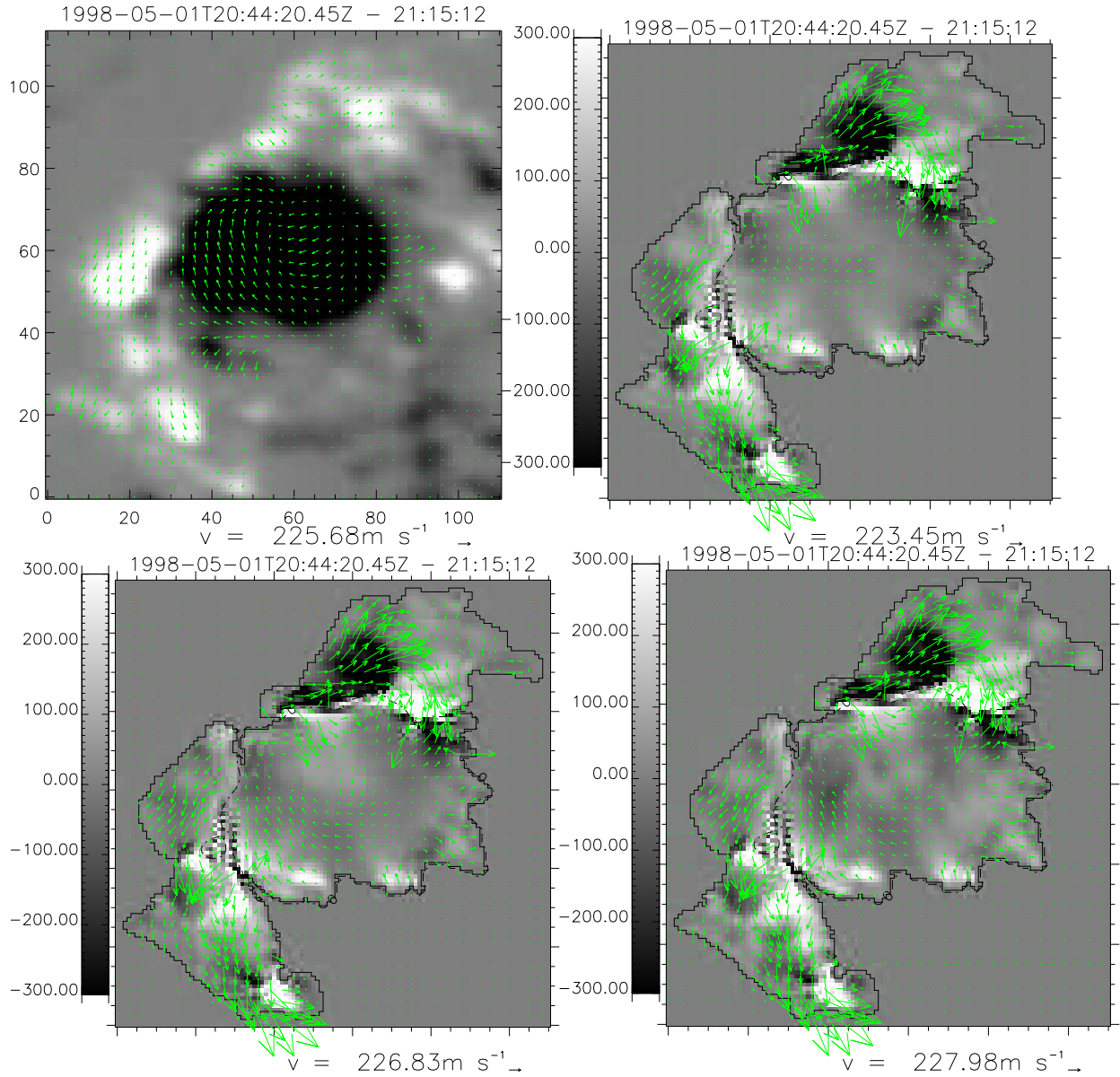


Fig. 12.— Same as Figure 11, but for different time.

magnetic field.

In order to examine how well the each method has followed the temporal variation in the magnetic field, we compare the temporal variation ( $\Delta B_z / \Delta t$ ) of the observed magnetic field reproduced using the inferred velocity in each combination. Figure 13(top left) shows the reproduced temporal variations using the MEF velocities, top right and bottom images

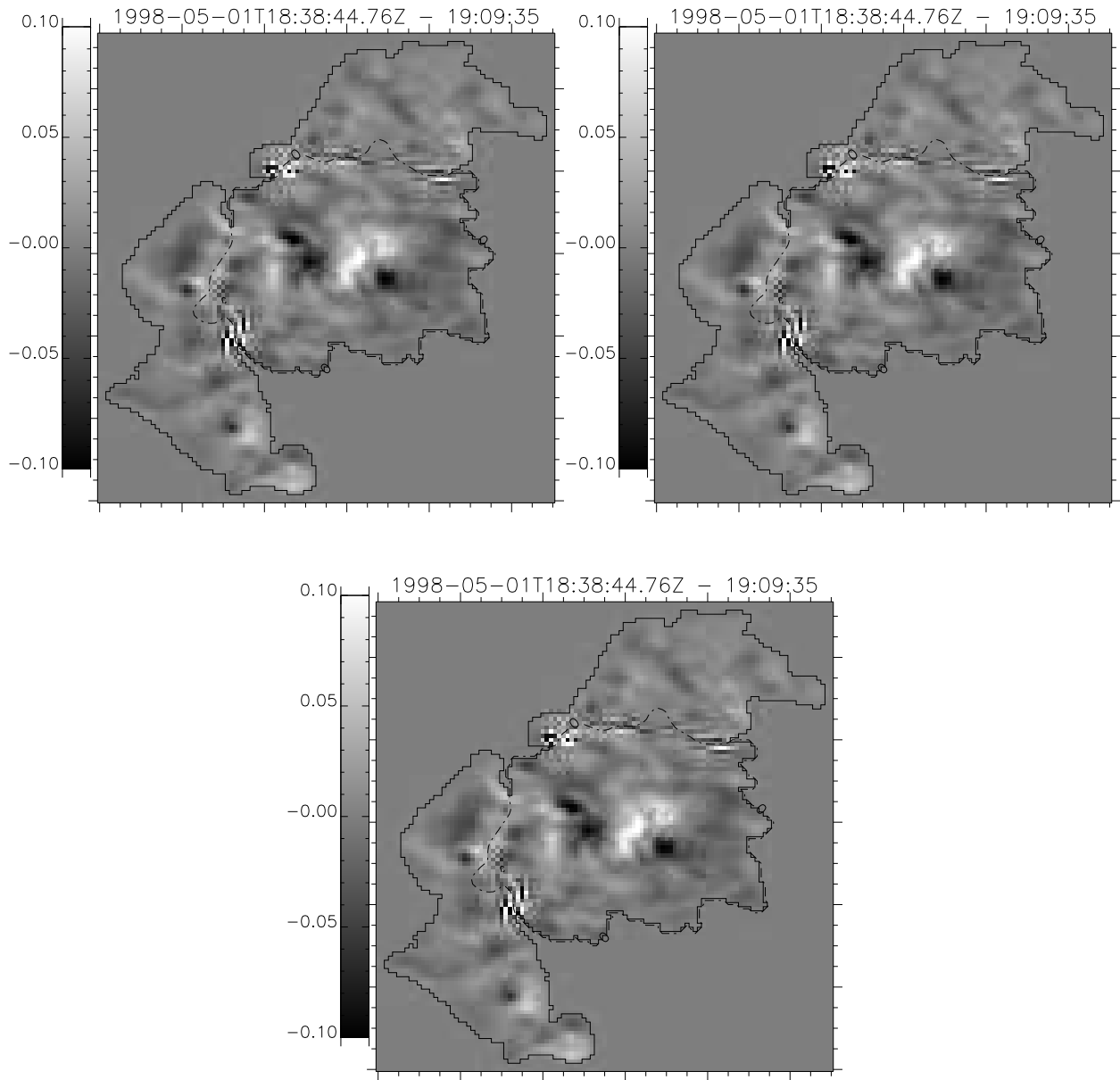


Fig. 13.— Maps of reproduced temporal variations computed using the velocity obtained from the MEF (top left), MEF+LCT (top right) and MEF+LCT+ $u_z$  (bottom) inversion techniques are shown.

are obtained by using the velocities of MEF+LCT and MEF+LCT+ $u_z$  techniques. A comparison of these maps with the observed temporal variation map (Figure 10 (right)) suggests that the reproduced maps match well in most places except near the PIL where erroneous high-frequency components reduces the correlation. Quantitatively, Figure 14 shows the scat-

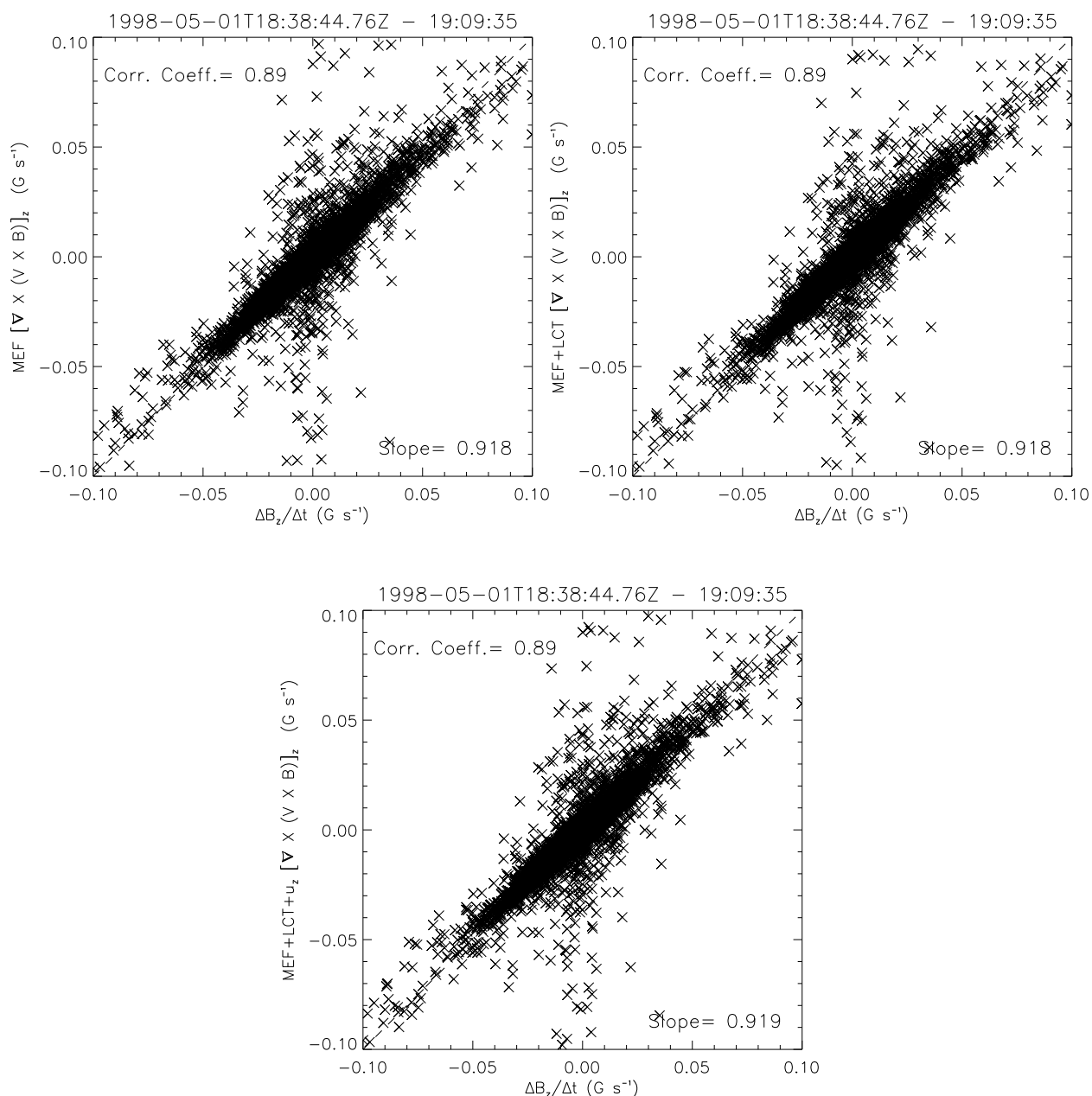


Fig. 14.— Scatter plots of reproduced temporal variation obtained by using the velocities from the MEF (top left), MEF+LCT (top right) and MEF+LCT+ $u_z$  (bottom) vs observed temporal variations are shown.

ter plot between the observed temporal variations and the reproduced temporal variations. Interestingly, all the reproduced (using MEF, MEF+LCT and MEF+LCT+ $u_z$ ) temporal variations show the same correlation, about 90%, with the observed temporal variations.

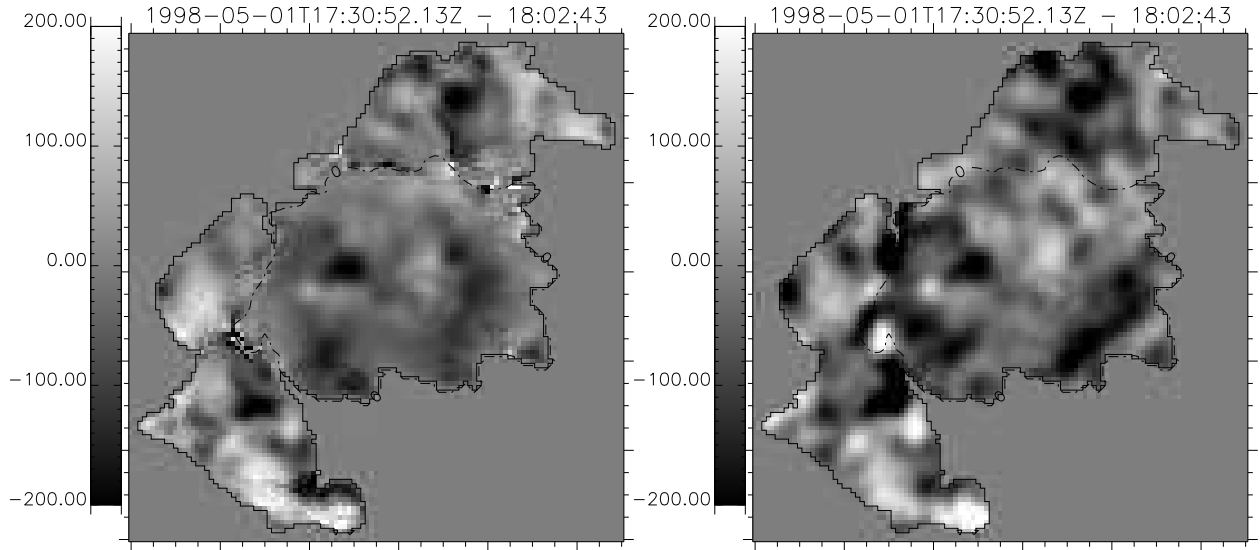


Fig. 15.— Left: A map of parallel component of the vertical velocity obtained from the MEF+LCT+ $u_z$  velocity inversion technique is shown. Right: A map of Doppler velocity obtained after removing the rotational gradient, p-mode oscillations and Evershed effect is shown.

As mentioned earlier, the MEF alone infers a velocity strictly perpendicular to the magnetic field. This is because flow parallel to the magnetic field does not affect the induction equation, but does increase the penalty function (4). On the other hand, Doppler velocity measurements can be used to constrain the parallel velocity field, and the results from MEF+LCT+ $u_z$  will include both parallel and perpendicular components. In order to examine this, we separated the parallel and perpendicular components of the vertical velocity. Figure 15 (left) shows the map of parallel component of the vertical velocity obtained from the MEF+LCT+ $u_z$ . The parallel velocity field obtained from the Doppler velocity is shown for comparison (Figure 15 (right)). A comparison of these two maps suggests that the parallel component of  $v_z$  obtained from the MEF+LCT+ $u_z$  varies more smoothly than the Doppler signal. There is, nevertheless, a good correlation between these two. This can be seen in the scatter plot between these two quantities (Figure 16 (left)). In the scatter plot it is noticeable that there is a good correlation between the two quantities with some scatter. At the same time the perpendicular component of the velocity is in close agreement with the vertical component of the velocity obtained from the MEF (Figure 16 (right)).

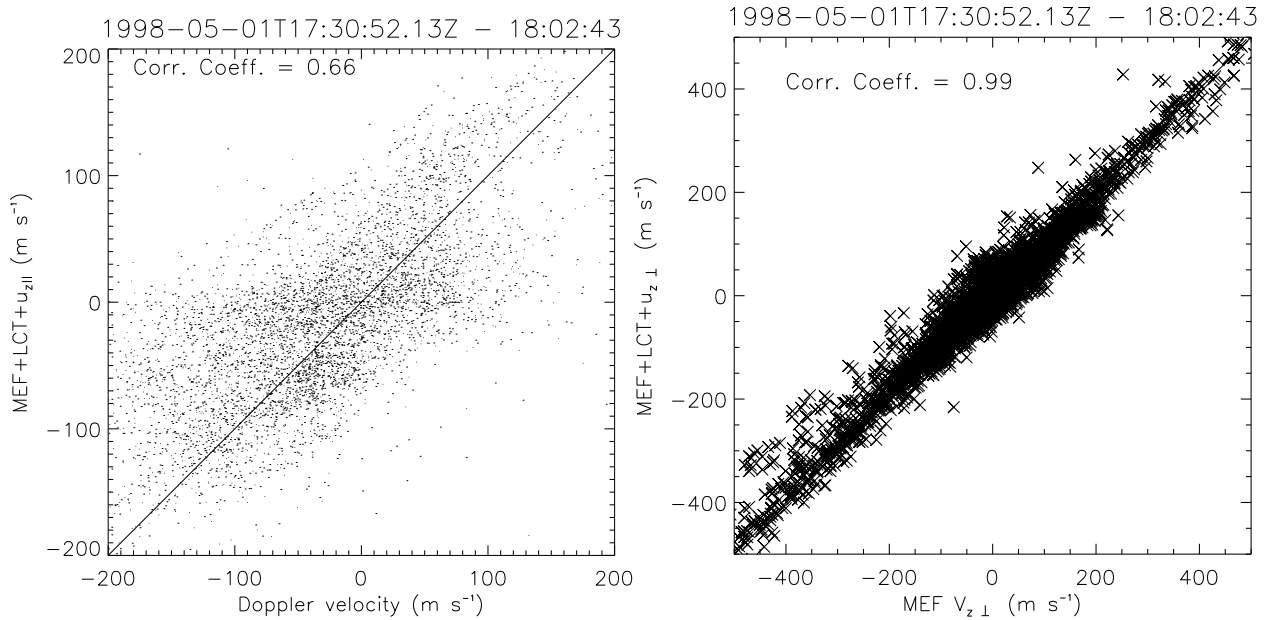


Fig. 16.— Left: A comparison of parallel component of the vertical velocity obtained from the MEF+LCT+ $u_z$  algorithm with the Doppler velocity is shown. Right: A perpendicular component of the vertical velocity obtained from the MEF+LCT+ $u_z$  is plotted against the vertical velocity inferred from the MEF algorithm.

#### 5.4. Energy and Helicity Fluxes

Figure 17 (bottom) shows the energy flux into AR 8210 as estimated by each of the different methods. It is notable that the estimates from MEF, MEF+LCT and MEF+LCT+ $u_z$  are all very similar to one another and different from the Poynting flux from LCT alone. That estimate is generally smaller and follows a different time history from the MEF-related estimates; different even from those that incorporate LCT as a constraint.

Time-integrating the Poynting flux energy yields an estimate of the energy injected into the whole active region (shown on top). The MEF+LCT+ $u_z$  curve, indicative of all the MEF-derived estimates, indicates that approximately  $11 \times 10^{31}$  ergs were stored during the five-hour observation. This is approximately twice the total energy estimate from LCT alone.

The main sunspot in the active region 8210 is rotating clockwise and the plage region on the East of it is rotating anti-clockwise. This rotation twists active region flux tubes thereby injecting helicity into the active region corona. Figure 18 (bottom) shows the helicity fluxes estimated using the various velocities. As with the Poynting flux, the estimates from MEF, MEF+LCT and MEF+LCT+ $u_z$  are all very similar and are notably different from the LCT

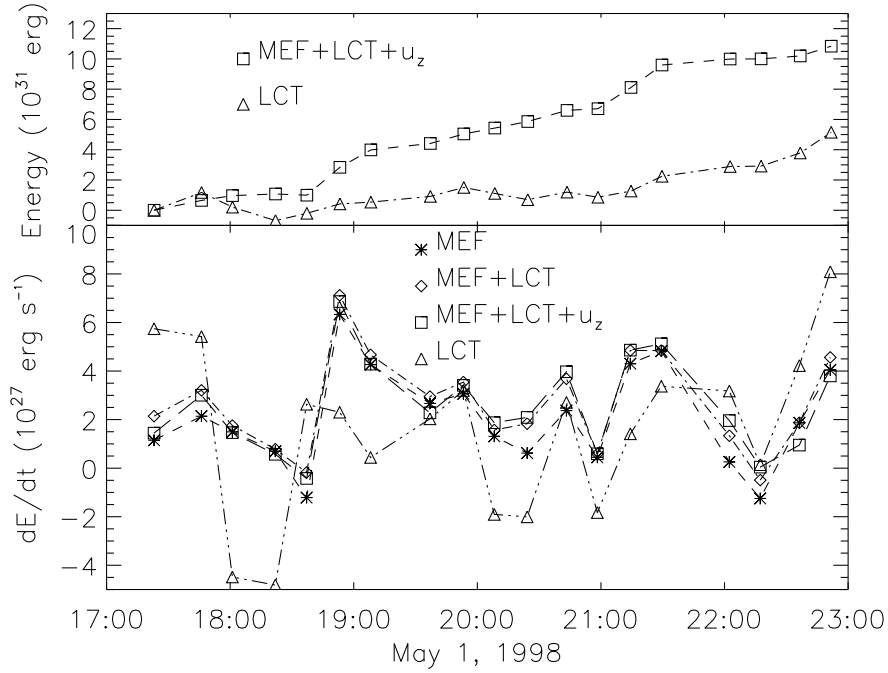


Fig. 17.— Bottom plot: The rate of energy flux estimated using various velocity inversion techniques is plotted as a function of time for the AR 8210. Top plot: The time integrated energy is plotted as a function of time.

alone. All four techniques agree that the helicity injection is generally positive (right-handed) consistent with the clockwise rotation of the dominant sunspot, and anti-clockwise relative motion of the opposing polarity. The LCT estimate is smaller than the other methods. Furthermore, the accumulated helicity, found from integrating the rate of change, is almost the same from all four methods  $\simeq 40 \times 10^{41} \text{ Mx}^2$  (although only the LCT and MEF+LCT+ $u_z$  are plotted).

The discrepancies between the LCT and the other methods can be understood by decomposing the helicity flux into contributions from shearing motion or the emergence/submergence. Figure 19 shows those two helicity flux components separately as a function of time for the velocity inferred from MEF+LCT+ $u_z$  and LCT. From the plot it is evident that although horizontal shearing motions are the main contributors in this case, the emergence/submergence contribution is not negligible. The LCT estimate of helicity from shearing does agree well with the hybrid estimate.

The MEF-derived Poynting flux and helicity flux differ from those derived from LCT alone. They do not, however, differ to the same degree in AR 8210 as they did in the

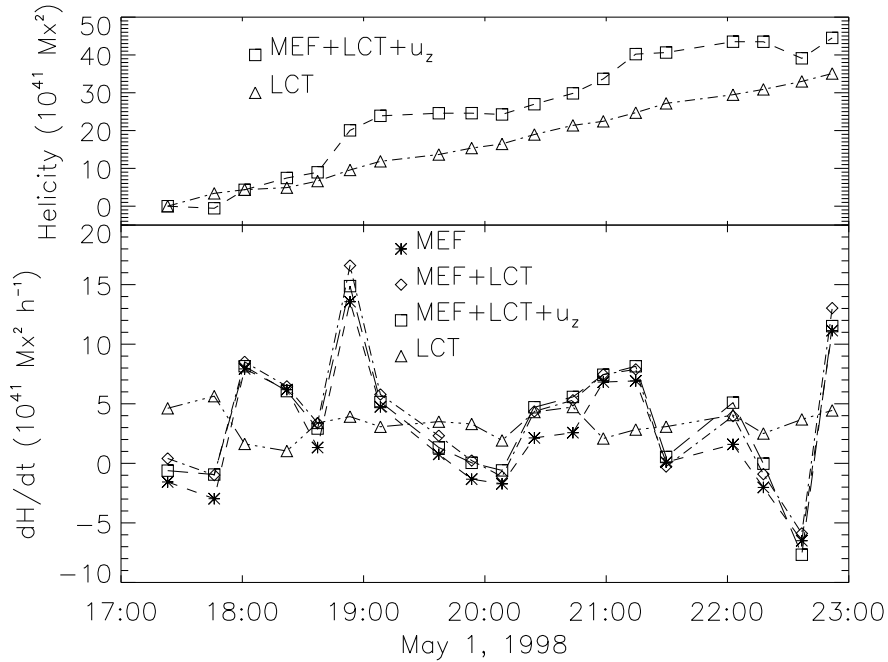


Fig. 18.— Bottom plot: The rate of helicity estimated using the various velocity inversion techniques is plotted as a function of time. Top plot: The time integrated helicity flux is plotted as a function of time.

test case presented in foregoing sections. This less pronounced difference may be due to the dominance of emergence in the test case and not in AR 8210. The test case showed that LCT is not well suited to estimating this component, and therefore cannot accurately estimate Poynting flux or helicity flux when it is significant. Even though it is not the dominant contributor to either energy or helicity, emergence is clearly playing some role. It is for this reason, we believe, that LCT consistently underestimates both energy and helicity in AR 8210. We also believe that the MEF-derived estimates, which agree with one another, and not with the LCT, provide the more accurate estimates.

## 6. Discussion

Each of the two auxiliary fields,  $\mathbf{u}_h$  and  $u_z$ , may be present or absent from the functional eq. (5). This leads to four possible versions of the MEF, namely (a) keeping  $\mathbf{u}_h$  and  $u_z$  zero, (b) introducing  $\mathbf{u}_h$  from LCT and keeping  $u_z$  zero, (c) introducing  $u_z$  from dopplergram and keeping  $\mathbf{u}_h = 0$  and (d) introducing  $\mathbf{u}_h$  from LCT and  $u_z$  from dopplergrams. In this study we have tested three of the possibilities, (a), (b) and (d), on synthetic vector magnetogram

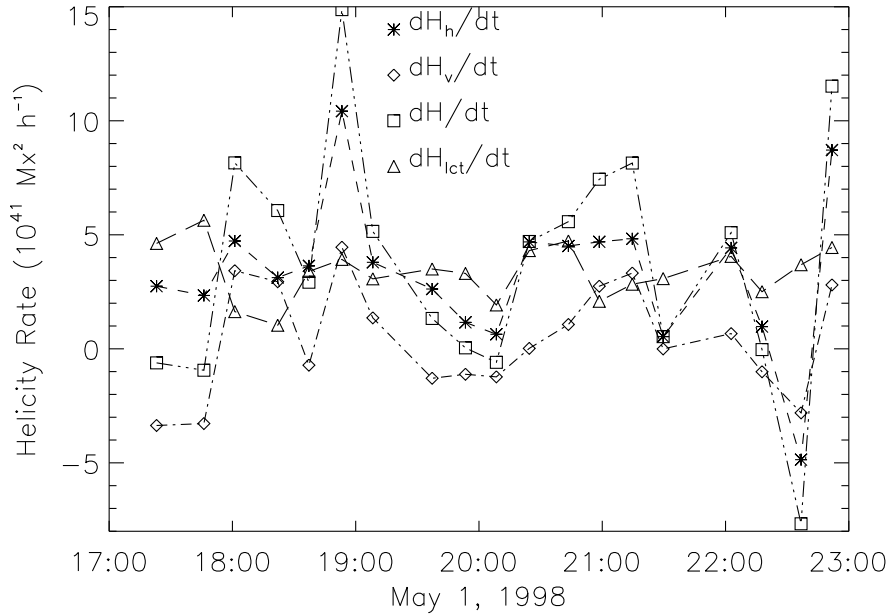


Fig. 19.— The total helicity flux ( $\square$ ), a component of helicity due to emergence/submergence ( $\diamond$ ) and shearing motion of magnetic footpoints ( $\star$ ) obtained by using the MEF+LCT+ $u_z$  velocity is plotted as a function of time. The helicity flux computed using the LCT velocity ( $\Delta$ ) is also plotted for comparison.

data sets, whose evolution and velocity field is known. Since the results of option (c) is similar to case (d), we have not included those results in this paper.

In order to test the capability of the constrained versions of MEF we applied each of them to a time series of evolving synthetic magnetograms whose velocity field is known. From these tests it is revealed that the MEF+LCT+ $u_z$  method best recovers the vertical flow field. This and all other methods recover the components of the horizontal velocity about equally well. The smallest velocity magnitude is obtained from the MEF method, perhaps as a consequence of selecting the smallest velocity from a set of consistent velocities.

We explored how each version performs when magnetograms are separated by increasing time intervals  $\Delta t$ . The performance is generally good when the time interval is small enough that the vertical field does not change significantly. Conversely, it appears that the algorithms' performances deteriorate at longer time interval. This suggests that the MEF and the hybrid methods can be performed on the magnetogram pairs which are separated by a small time interval, smaller than the evolutionary time scale of active region, typically less than an hour.

In solar physics, the photospheric velocity is used to compute integral quantities like the energy flux and helicity flux, characterizing the evolution of the magnetic field. None of our methods recovered the net vertical flow well, however, the MEF+LCT+ $u_z$  estimate is about 50% larger than the true net vertical flow at small time interval. It is possibly due to the reasonable performance on vertical velocity that it also recovers well the Poynting flux. The other method of the MEF also performed well in recovering the Poynting flux. LCT alone did not perform well in estimating the Poynting flux as its magnitude is one order smaller than the true Poynting flux.

The synthetic magnetograms come from MHD simulation of a magnetic flux rope rising through a convection zone. This scenario means that the emerging term, containing  $v_z$ , is the dominant contributor to the helicity flux. The helicity fluxes obtained from the LCT velocities turn out to be an order of magnitude too small. This implies that the  $v_z$  contribution to  $\mathbf{u}_h$  is absent or too small in the LCT velocity. It also appears that the LCT under-estimates the contribution due to shearing motion. On the other hand, the total helicity flux computed using the MEF velocity is in good agreement with the true helicity flux, owing mostly to its reasonably good recovery of the vertical velocity. The MEF method finds a shearing component is negative as opposed to the true shearing component of the helicity flux. This is another consequence of the minimization method to select the smallest velocity field. On the other hand, the hybrid method performed well in estimating the helicity fluxes due to the shearing motion and flux emergence with correct sign at smaller time interval. All these results suggest that the hybrid method is better than just using the MEF or LCT alone.

All methods were also capable of inferring velocity fields from IVM data of AR 8210. Even though the MEF method failed to show the clockwise rotation of the sunspot in AR 8210, the Poynting fluxes and helicity fluxes obtained from the MEF and its hybrid methods are similar in magnitude.

A similar data sets from IVM for the AR 8210 is used by Régnier & Canfield (2006), but their analysis is different than ours in the following way: (1) We used a longer time series (2) They used only the transverse components of the MEF velocity to estimate the Poynting fluxes (3) They used the NLFF method to estimate the coronal magnetic field and the helicity fluxes. (4) The region used to estimate the velocity and helicity fluxes are larger in Régnier & Canfield (2006), compared to ours. In spite of this, the accumulated energy computed using the LCT horizontal velocity is of about  $5.5 \times 10^{31}$  ergs and it is close to the free energy budget ( $1-5 \times 10^{31}$  ergs) obtained by Régnier & Canfield (2006) using NLFF method. At the same time the energy accumulated by the active region computed using the MEF and its hybrid method is about  $11 \times 10^{31}$  ergs, almost double the value obtained using

LCT velocities.

The rate of helicity estimated using the LCT and MEF method is positive and comparable to values found by Moon et al. (2002b); Nindos et al. (2003) using the MDI data sets. Nindos et al. (2003) also found the chirality of the active region and the helicity of the ejected cloud to be positive. Our own estimation of the accumulated helicity over a period of 6 hr using the LCT and MEF velocities is also positive and it is about  $35 \times 10^{41}$  and  $45 \times 10^{41}$   $\text{Mx}^2$  respectively. Similar results were obtained by Pariat et al. (2006) using a  $G_\theta$  method and LCT velocities. The helicity fluxes due to the shearing motion of magnetic field footpoints obtained from our own hybrid methods of MEF is positive and the values are in close resemblance with the helicity fluxes obtained by using LCT velocity.

Recently, there are many other methods have been developed to infer the horizontal velocities of the magnetic footpoints at one level (e.g. Schuck (2006)). In our own study of velocity inversion technique, we introduced the horizontal velocity obtained from the LCT. In future we would also explore the possibility of introducing the velocity obtained from DAVE (Schuck 2006) which is one of the best methods in recovering the horizontal velocity magnitude and direction (Welsch et al. 2007). The continuum image, G-Band and CN-band images shows motions on very fine scales within sunspots. The velocity obtained by applying the LCT technique on these images is good proxy for partial velocity information for the MEF method.

The Doppler data used in the AR 8210 is not a complete representation of the vertical flow as in the ANMHD data, which includes both field-aligned and perpendicular components. The Doppler data is almost the field aligned data which does not change the magnetic field strength. The estimated Poynting flux and helicity fluxes in AR 8210 using the MEF combined with the Doppler velocity suggested that they differ slightly compared to MEF alone. This indicates that most of the Doppler velocity is field-aligned velocity which will not contribute to the helicity fluxes.

As the dopplergrams and magnetograms are obtained from the inversion of the spectral line data, application of LCT on these datasets should give a similar velocity field. But one represents a mixture of magnetized and non-magnetized plasma velocity and the later represents the magnetic footpoint velocity. Recently some measurements of the magnetized plasma velocities have been made using the Stokes Q and U profiles (Chae et al. 2004). The dopplergrams made by using such information along with the LCT velocities obtained from the same dopplergrams can be used as a partial magnetic footpoint velocity information for the MEF algorithms. We also intend to use the Doppler velocity obtained from the so-called V-crossing measurement. This has better signal-to-noise ratio than the Q and U signal. The observed velocities are the plasma velocity in the magnetic field regions. Using these

velocities we expect that the MEF algorithm infers the 3 components of the velocity which closely approximates the photospheric velocity.

The Stokes signal obtained from the ground based telescopes are always affected by the atmospheric seeing effects unless one corrects it by higher order adaptive optics system. Such atmospheric effects will affect the magnetic field measurements and hence  $\partial B_z/\partial t$ . This will propagate into the velocity field measurements. We do not know at this stage how much uncertainty is introduced in the measured velocities by atmospheric effects. We also do not know how our MEF algorithm behaves when the  $180^\circ$  ambiguities are not fully resolved. We would like to undertake these measurements using space based data from Solar Optical Telescope (SOT Tsuneta et al. 2007) and HMI on SDO in near future.

## 7. Acknowledgment

We would like to thank the anonymous referee for his/her comments/suggestions, which improved the manuscript. B.R would like to thank Brian Welsch and George Fisher for providing the FLCT code used in this work. Thanks also to K.D. Leka for providing the IVM vector magnetograph data. This work is supported by NSF SHINE program. W. P. A. was supported in part by NASA's Heliophysics Theory Program, and NSF's Center for Integrated Space Weather Modeling.

## REFERENCES

- Abbett, W. P., Fisher, G. H., & Fan, Y. 2000, *ApJ*, 540, 548
- Abbett, W. P., Fisher, G. H., Fan, Y., & Bercik, D. J. 2004, *ApJ*, 612, 557
- Berger, M. A. 1984, *Geophys. Ap. Fluid Dyn.*, 30, 79
- Canfield, R. C., et al. 1993, *ApJ*, 411, 362
- Chae, J. 2001, *ApJ*, 560, L95
- Chae, J., Moon, Y.-J., & Pevtsov, A. A. 2004, *ApJ*, 602, L65
- Démoulin, P., & Berger, M. A. 2003, *Solar Phys.*, 215, 203
- Domingo, V., Fleck, B., & Poland, A. I. 1995, *Solar Phys.*, 162, 1
- Evershed, J. 1909, *MNRAS*, 69, 454

- Fan, Y., Zweibel, E. G., Linton, M. G., & Fisher, G. H. 1999, *ApJ*, 521, 460
- Fisher, G. H., & Welsch, B. T. 2007, ASPC (in press)
- Hart, A. B. 1954, *MNRAS*, 114, 17
- Hathaway, D. H., Beck, J. G., Bogart, R. S., Bachmann, K. T., Khatri, G., Petitto, J. M., Han, S., & Raymond, J. 2000, *Solar Phys.*, 193, 299
- Labonte, B. J., Mickey, D. L., & Leka, K. D. 1999, *Solar Phys.*, 189, 1
- Leka, K. D., & Barnes, G. 2003, *ApJ*, 595, 1277
- Libbrecht, K. G., & Zirin, H. 1986, *ApJ*, 308, 413
- Longcope, D. 2004, *ApJ*, 612, 1181
- Mickey, D. L., Canfield, R. C., LaBonte, B. J., Leka, M. F., K. D. Waterson, & Weber, H. M. 1996, *Solar Phys.*, 168, 229
- Moon, Y.-J., Chae, J., Choe, G. S., Wang, H., Park, Y. D., Yun, H. S., Yurchyshyn, V., & Goode, P. R. 2002a, *ApJ*, 574, 1066
- Moon, Y.-J., Chae, J., Wang, H., Choe, G. S., & Park, Y. D. 2002b, *ApJ*, 580, 528
- Nindos, A., Zhang, J., & Zhang, H. 2003, *ApJ*, 594, 1033
- November, L. J., & Simon, G. W. 1988, *ApJ*, 333, 427
- Pariat, E., Nindos, A., Démoulin, P., & Berger, M. A. 2006, *A&A*, 452, 623
- Pohjolainen, S., et al. 2001, *ApJ*, 556, 421
- Ravindra, B., & Longcope, D. W. 2007, *J. Astrophys. Astr.* (submitted)
- Régnier, S., & Canfield, R. C. 2006, *A&A*, 451, 319
- Scherrer, P. H., et al. 1995, *Solar Phys.*, 162, 129
- Schuck, P. W. 2006, *ApJ*, 646, 1358
- Stenflo, J. O. 1994, *Astrophysics and Space Sciences Library*, Vol. 189, *Solar Magnetic Fields. Polarized radiation diagnostics* (Kluwer Academic Publishers)
- Sterling, A., & Moore, R. L. 2001, *JGR*, 106, 25,227

- Tsuneta, S., et al. 2007, *Solar Phys.* (submitted)
- Wang, T., Yan, Y., Wang, J., Kurokawa, H., & Shibata, K. 2002, *Solar Phys.*, 572, 580
- Warmuth, A., Hanslmeier, A., Messerotti, M., Cacciani, A., Moretti, P. F., & Otruba, W. 2000, *Solar Phys.*, 194, 103
- Welsch, B. T., et al. 2007, *ApJ* (in press)
- Welsch, B. T., & Fisher, G. H. 2007, *ASPC* (in press)
- Welsch, B. T., Fisher, G. H., Abbett, W. P., & Regnier, S. 2004, *ApJ*, 610, 1148
- Xia, Z.-G., Wang, M., Zhang, B.-R., & Yang, Y.-H. 2002, *Chinese Astron. and Astrophys.*, 26, 164